DE TTK

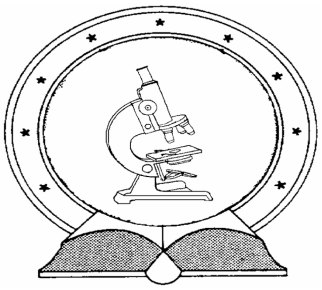

1949

# Fracture and fragmentation of disordered materials

PhD Thesis
Egyetemi doktori (PhD) értekezés

Gábor Timár

Supervisor / Témavezető
Dr. Ferenc Kun

University of Debrecen
PhD School in Physics

Debreceni Egyetem
Természettudományi Doktori Tanács
Fizikai Tudományok Doktori Iskolája

Debrecen
2012

**Prepared at**
the University of Debrecen
PhD School in Physics
and
the Department of Theoretical Physics

**Készült**
a Debreceni Egyetem Fizikai Tudományok Doktori Iskolájának
Szilárdtestfizika és anyagtudomány programja keretében a Debreceni
Egyetem Elméleti Fizikai Tanszékén

Ezen értekezést a Debreceni Egyetem Természettudományi Doktori Tanács Fizikai Tudományok Doktori Iskolája Szilárdtestfizika és anyagtudomány programja keretében készítettem a Debreceni Egyetem természettudományi doktori (PhD) fokozatának elnyerése céljából.

Debrecen, 2012. Timár Gábor

Tanúsítom, hogy Timár Gábor doktorjelölt 2008-2012 között a fent megnevezett doktori iskola Szilárdtestfizika és anyagtudomány programjának keretében irányításommal végezte munkáját. Az értekezésben foglalt eredményekhez a jelölt önálló alkotó tevékenységével meghatározóan hozzájárult. Az értekezés elfogadását javaslom.

Debrecen, 2012. Dr. Kun Ferenc
témavezető

# Fracture and fragmentation of disordered materials

Értekezés a doktori (PhD) fokozat megszerzése érdekében a fizika tudományágban

Írta: Timár Gábor, okleveles fizikus

Készült a Debreceni Egyetem Fizikai Tudományok Doktori Iskolája Szilárdtestfizika és anyagtudomány programja keretében

Témavezető: Dr. Kun Ferenc

A doktori szigorlati bizottság:

elnök: Dr. ..... .....
tagok: Dr. ..... .....
Dr. ..... .....

A doktori szigorlat időpontja: 2011. december 16.

Az értekezés bírálói:

Dr. ..... .....
Dr. ..... .....

A bírálóbizottság:

elnök: Dr. ..... .....
tagok: Dr. ..... .....
Dr. ..... .....
Dr. ..... .....
Dr. ..... .....

Az értekezés védésének időpontja: 2012. .....

# Contents

# Chapter 1

# Introduction

A clear understanding of the fracture phenomena of various types of materials is essential in modern engineering, therefore the physics of fracture has been in the focus of intensive research in recent decades. Fracture, i.e. the separation of a body into two or more pieces under the action of stress, can occur in many different ways depending on the loading method and geometrical conditions.

In a more specific sense fracture usually refers to phenomena where the sample splits into two parts with the propagation of a well defined crack in between. The brittle fracture of materials has two substantially different scenarios depending on the amount of structural disorder: for homogeneous materials such as crystalline solids at the critical stress a single crack is formed which propagates in an unstable manner. However, in materials with a high degree of heterogeneity fracture develops progressively, i.e. under an increasing external load first microcracks nucleate at local weaknesses which may then undergo several steps of growth and arrest. Finally macroscopic fracture occurs as the culmination of the gradual accumulation of damage. The nucleation and growth of cracks is accompanied by the emission of elastic waves which can be recorded in the form of acoustic noise. In ferromagnetic materials the shifting and sudden change of orientation of magnetic domains due to microcracking activity also gives rise to magnetic noise. Measuring acoustic and magnetic emission (AE and ME) is the primary source of information on the microscopic dynamics of the damaging and fracture of heterogeneous brittle materials. Experiments of the past two decades have reported that the fracture of such materials is

generally accompanied by crackling noise which has a scale-invariant structure, i.e. the probability distributions of the energy of breaking bursts and the waiting times between them both follow power-law behaviour with the exponent showing dependence on loading conditions and material properties such as ductility. Understanding the mechanisms behind crackling noise may provide valuable information on the integrity of structural components in engineering and may even enable us in some cases to foresee imminent failure.

Fragmentation is a substantially different form of breakup, where a sample breaks into many small pieces due to a large amount of energy suddenly imparted to the system. Fragmentation occurs in nature on a huge variety of length scales, ranging from the breakup of heavy nuclei through geological phenomena to supernovae. It also forms the basis of a number of industrial applications such as crushing, milling and grain liberation techniques, therefore a lot of scientific effort for over half a century has been put into studying such processes. A striking result of most fragmentation experiments on heterogeneous brittle materials is that the fragment mass distribution follows a power-law behaviour with an exponent independent of the amount or form of imparted energy and material type. The universal exponent proved to be mainly determined by the dimensionality of the system. A number of studies showed that the behaviour of a system near the fragmentation threshold energy resembles that of critical systems where some important quantities diverge or go to zero at the critical point. These findigs imply that fragmentation processes may be considered analogous to continuous phase transitions and accordingly universality classes of fragmentation may be identified.

During my Ph.D. studies I investigated the fracture and fragmentation of heterogeneous materials by means of computer simulations of realistic discrete element models. I concentrated on analyzing the crackling noise emerging in single crack propagation in a two-dimensional rectangular specimen subject to three-point bending conditions. For this purpose a two-dimensional discrete element model (DEM) was used, consisting of randomly shaped convex polygons to capture the granular structure of the material. I carried out simulations applying a constant low strain rate and analyzed statistically the various features of the propagating crack. The main focus of

my study was identifying and characterizing the bursts in crack propagation that correspond to crackling noise in experiments. In my DEM approach I was able to reproduce the scale-invariant structure of the distributions of various important quantities related to bursts, as seen in experiments. My simulations also provide a better understanding of the spatial structure of microcrackings in front of the propagating crack. In addition to crack propagation, I carried out a detailed study of the impact fragmentation of spheres by using a three- dimensional discrete element model. In this case a random packing of spherical particles was used to model the structure of heterogeneous materials. My goal was to achieve a better understanding of the fragmentation phase transition. I showed that the exponent of fragment mass distributions is independent of the impact velocity. I carried out a finite size scaling analysis to numerically obtain the critical exponents of the transition. I also derived novel scaling laws regarding the impact velocity dependence of the damage and damage rate in brittle materials. As an extension of the existing discrete element model I introduced new features that enabled me to simulate the impact of plastic spheres. I found that the impact fragmentation of such materials is substantially different from that of brittle ones. Most importantly the exponent of the fragment mass distribution proved to be significantly smaller than in the brittle case, suggesting that the fragmentation of plastic materials belongs to a universality class different from that of brittle materials. This striking prediction was confirmed by the impact fragmentation experiments we carried out on small polypropylene particles.

The structure of the thesis is as follows: Chapter 2 gives an overview of fracture and fragmentation phenomena, summarizing the most important experimental findigs and theoretical studies with special attention to the most successful simulation methods in the field. I give a more detailed introduction to discrete element models and molecular dynamics simulations. As an example, I present the details of a particular DEM, that I used to study the properties of crackling noise in single crack propagation. In Chapter 3 I present the results of my studies on crackling noise. Chapter 4 gives a detailed overview of the three-dimensional model used to simulate the impact of heterogeneous brittle materials and I discuss my results regarding the analysis of the fragmentation process. In Chapter 5 I give an overview

of the techniques used in performing impact fragmentation experiments of polypropylene particles followed by a summary of the most interesting experimental results. I then present the model extensions I proposed to simulate the impact of plastic spheres and discuss my numerical results which are in very good agreement with the experiments.

# Chapter 2

# Fracture and fragmentation

This chapter gives a basic overview of the scientific literature regarding fracture and fragmentation phenomena, listing the most significant experimental and theoretical studies. I give a more detailed description of simulation techniques used in the fields, with special attention to results that are important from the point of view of my research.

## 2.1 Fracture

Fracture generally refers to the separation of a body into two parts due to the application of stresses. Fracture phenomena may be categorized in numerous ways, e.g. according to the dimensionality of the sample, geometrical conditions, material properties or the method of stress-application.

It is a well-known fact that fracture occurs in solids at much lower stresses, than what can be deduced from simple solid state physics estimations of crystalline structures. In most materials the ratio of estimated to observed fracture strength is around two or three orders of magnitude. This discrepancy can be easily resolved with the assumption that the stress-field inside the body can never be homogeneous due to the disordered nature of all materials under normal conditions. The characteristic length scale of disorder can vary greatly. Microscopically disorder can mean for example vacancies, inclusions, dislocations. Larger scales of disorder are involved in the structure of composites or granular materials like ceramics or concrete. Disorder can be in motion: dislocations can migrate, microcracks can form and heal, interstitials can diffuse, etc. When dealing with the fracture or

fragmentation of solids however, the time scale of the fluctuations of the relevant type of disorder is always very large compared to the time scale of the process investigated. In this case disorder is called "quenched" and can be considered time-independent [1]. Due to the presence of disorder the stresses inside a loaded specimen are concentrated around weak spots such as flaws, grain boundaries, triple points, causing fractures to initiate there. Griffith [2, 3] used this assumption to derive his classic criterion for crack propagation in brittle materials in static or quasi-static conditions. His results have excellent agreement with experiments of brittle materials, that can be considered homogeneous. This marks the beginning of the development of fracture mechanics. Modifications of Griffith's theory to include the plastic zone developing at the crack tip were made by Irwin [4, 5], while Bazant [6] made generalizations for quasi-brittle materials. Linear elastic fracture mechanics (LEFM) and elastic-plastic fracture mechanics (EPFM) have had huge success in predicting the behaviour of various different materials commonly used in engineering, however these theories are not applicable to highly disordered materials and cannot deal with problems such as fracture due to creep, fatigue or the emergence of crackling noise. Explaining these phenomena requires a thorough understanding of the dynamics of the nucleation and correlation of cracks in disordered media.

### 2.1.1 Crackling noise

Materials of low disorder typically fail due to the sudden initiation and rapid propagation of one single crack [7]. The fracture of highly disordered materials however occurs progressively [8, 9]. As stress is applied, first uncorrelated micro-cracks nucleate throughout the volume of the sample at points of high stress concentration, typically due to flaws near grain boundaries. Increasing the load will cause the existing micro-cracks to grow while new nucleations continue to occur. Approaching the critical stress results in localization in the form of one single growing crack along which the specimen falls apart.

When cracks nucleate or propagete, elastic energy is dissipated mainly in creating new crack surface but also due to heating and by altering the structure of the material near the crack surface. As is the case in driven dissipative systems in general, the energy dissipation rate is a highly irregular function [10]. This is caused by the fact that energy is generally

dissipated in avalanches of correlated microscopic fracture events. Such an avalanche or breaking burst causes the emission of elastic waves that can be measured in experiments as acoustic signals, reffered to as crackling noise. This phenomenon is abundant in nature and has been observed in a variety of materials subject to various different forms of external driving. The energy scales involved in processes producing crackling noise range over many orders of magnitude.

### 2.1.2 Experimental findings

Crackling noise occurs in many different scenarios in driven dissipative systems [11]. A typical example is the Barkhausen noise arising in ferromagnetic materials driven by a slowly varying magnetic field or by applying a slowly increasing strain. Barkhausen noise can be measured in the form of acoustic and magnetic emission caused by rapid changes in the domain structure [12, 13, 14]. The acoustic emission of disordered solids subjected to quasi-static loading was intensively studied in Refs. [15, 16, 17, 18]. The plastic deformation of some crystals has also been shown to produce crackling noise due to the jerky behaviour of slip-mechanisms involved in the process [19]. This phenomenon has even been found in superconductors where avalanches of superconducting vortices were investigated [20]. A common observation for such systems is that the structure of crackling noise is found to be scale-invariant, i.e. the probability distributions of the sizes of measured avalanches and the waiting times between two successive events have a power-law form.

Understanding the statistical properties of crackling noise is extremely important from the point of view of fracture phenomena, as it provides valuable information on the microscopic dynamics of the initiation and propagation of cracks. In recent decades, measuring the acoustic emission (AE) of stressed solids has been the major form of investigations regarding the emergence of crackling noise. In Ref. [16] Petri et al. presented results of uniaxial loading experiments on laboratory samples of synthetic plaster. They found power-law distributions of the amplitudes of bursts and also waiting times in the measured AE spectra. They suggested that the self-similarity in crackling noise is a manifestation of self-organized criticality (SOC), as the system seems to be in a stable critical state without any control parameter.

Maes et al. reported results of AE measurements in creep experiments performed on cellular glasses [15]. They found that the AE signal consists of bursts with power-law distributed amplitudes and waiting times. They also analyzed spatial correlations and observed that the distance between two consecutive events also shows scale invariance. In Ref. [21] tensile and creep tests on polyurethane foams were analyzed by Deschanel et al. by measuring AE signals. They showed that the energy of bursts and waiting times are power-law distributed in every case and that the exponent for energies shows a striking universality in the sense that it proved to be independent of material property and loading conditions. By performing experiments at various different temperatures (thus controlling the mechanical response of the samples) they found that the scaling exponents of energies and waiting times are much more strongly related to mechanical behaviour than the microstructure of the material. Salminen et al. reported results of crackling noise produced by the tensile fracture of paper sheets [17], where they found power-law distributed energies and waiting times in AE spectra. Recently the crackling noise arising in the dynamic fracture of steel specimens was investigated in Ref. [22]. The so-called Charpy impact test was used in the experiments, which is a common method in engineering to determine fracture toughness of materials. As a crack propagates in a ferromagnetic material, the opening up of the crack causes magnetic flux leakage. In this way the jerky movement of the crack tip results in rapid changes of the magnetic flux. These changes can be transformed to voltage in an appropriately placed coil, thus making it possible to record magnetic emission (ME) spectra. Bursts in dynamic crack propagation were analyzed that correspond to peaks in the recorded voltage. It was found that the amplitude, area and energy of voltage peaks are all power-law distributed with exponents independent of the hammer impact velocity. However they found clear dependence of the exponents on the mechanical behaviour, i.e. the ductility of the sample. Niccolini et al. performed flexural loading experiments in a three-point bending geometry on fiber reinforced concrete samples and analyzed the waiting times between successive AE events [23]. They found that the distribution of waiting times $T$ follows a scaling law of the form

$$P(T) \sim Rf(RT), \tag{2.1}$$

where $R$ denotes the mean rate of events in the time window considered. This scaling behaviour was found by Corral [24] to describe earthquake time series with good quality.

In light of the documented magnitudes and occurrance times of earthquakes, it has been a long standing argument, that seismic activity, like crackling noise, shows self-organized criticality. The Gutenberg-Richter law of the magnitudes of earthquakes and the Omori law of aftershock times show scale-invariant behaviour similarly to the power-law distributions of energies and waiting times observed in AE and ME in fracture experiments. Experimental results presented in Refs. [23, 25] further enforce the analogy between crackling noise in fracture and earthquake time series.

### 2.1.3 Theoretical approaches

Due to the complicated nature of the problem of fracture in disordered solids, the possibilities of pure analytical approaches in this field are rather limited. Most theoretical investigations rely on numerical simulations of discrete stochastic models. An important branch of such models can be classified as lattice models, of which the random fuse model (RFM) has proved to be the most successful, introduced by Arcangelis et al. [26]. This approach models breaking processes by the break-down of a network of fuses under an increasing external voltage or current. Initially a regular lattice is considered, where bonds are either fuses, with probability $p$, or insulators, with probability $1-p$. The value of $p$ is chosen to be larger than the percolation threshold, therefore the network of fuses is a spanning cluster on the given lattice. An external voltage is applied across the network, and the voltages at each node are calculated. The fuse with the highest voltage difference, i.e. the hottest fuse is identified and turned into an insulator (it burns out). After every burning event the voltages are recalculated, and the new hottest fuse is identified, then removed. This procedure is continued until a dividing crack emerges, i.e. the cluster of fuses is no longer a spanning cluster. Figure 2.1 shows a lattice of fuses without random dilution, i.e. $p = 1$, where some fuses have already burned out.

Such an electrical network is the scalar analog of a network of elastic beams, where the burning out of individual fuses as the external voltage is increased corresponds to the physical breaking of beams as a result of

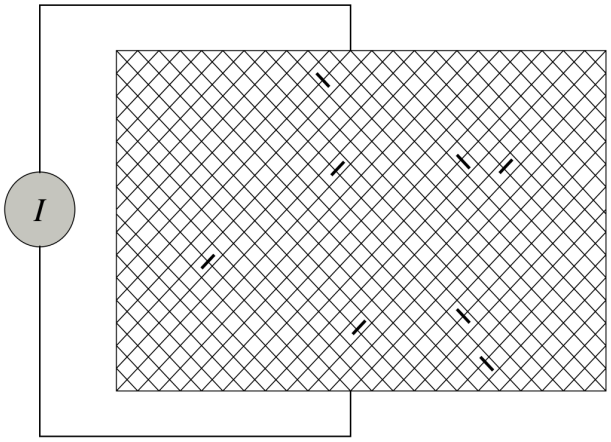


Figure 2.1: A network of fuses in the random fuse model with fuse probability $p = 1$, i.e. all bonds are fuses initially. The system is loaded by slowly increasing the current $I$ between the bus bars. The figure shows a state of the system when some fuses have already burned out.

increasing mechanical stress [26]. RFM-type approaches provide a simple understanding of many features of fracture processes in disordered, quasi-brittle materials.

Zapperi et al. investigated the structure of crack surfaces in a two-dimensional random fuse model and found a universal roughness exponent [27]. They also observed, that macroscopic failure is preceeded by avalanches of fuses burning out, with the size distribution of such avalanches also following universal power-law behaviour. In Ref. [28] Alava et al. studied the size dependence of the strength of disordered materials with a flaw via a two-dimensional RFM. In the limit of large flaw size, they confirmed, that LEFM gives a good approximation of fracture strength, however for smaller flaws they showed that the presence of a fracture process zone (FPZ) determines the size effects. The process zone refers to a cloud of microcracks (burnt out fuses) in areas of high stress concentration, near the crack tip. Their simulations showed that the process zone plays a key role in determining crack propagation in highly disordered materials. An exponential decay of the damage profile along the crack axis was found. Their results regarding the size scaling of material strength proved to be in very good agreement with experiments on the fracture of paper sheets with flaws [28].

An other class of stochastic models that has been intensively studied is

the so-called fiber bundle model (FBM) [29, 30, 31, 32, 33, 34, 35]. This approach models the strained specimen as a bundle of elastic fibers usually with a constant Young's modulus, but varying breaking thresholds. As an increasing force $F$ is applied to the bundle, all the fibers gradually become increasingly elongated, until the point when the weakest of the fibers breaks. The bundle as a whole however has to equal the force $F$, so the load carried by the broken fiber is redistributed among the intact fibers. This might result in some further fiber breakings. After the system stabilizes, $F$ can be further increased until another fiber is broken. The procedure is continued until all the fibers in the bundle are broken. In the original formulation of the model, the extra load of broken fibers is redistributed equally among all the remaining fibers [18, 29]. This type of FBMs is called equal or global load sharing (ELS or GLS) FBM. This approach corresponds to mean-field methods in statistical physics, and is simple enough in some cases to yield analytic results. Actually the ELS FBM is exactly the mean field version of the RFM.

An ELS fiber bundle is depicted in Fig. 2.2, where the rigidity of the loading bars ensures that no stress fluctuation can arise.

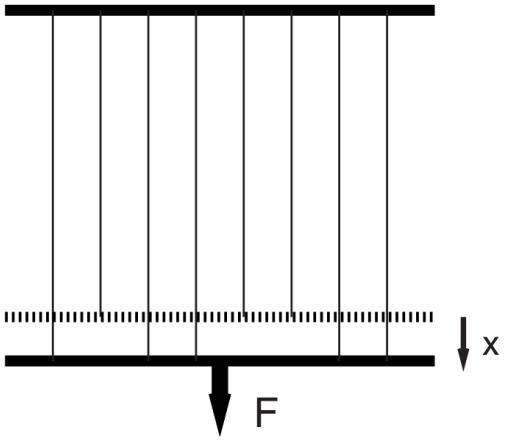


Figure 2.2: Schematic representation of the equal load sharing fiber bundle model. A force $F$ is applied to the bundle, due to which all the fibers become strained. Weak fibers break and the load is then redistributed equally on all the remaining fibers.

Another type of FBMs, which is more realistic in many cases, is the so-called local load sharing (LLS) fiber bundle model [18, 30, 36]. In this case,

the load of broken fibers is redistributed only among nearby fibers according to a decay function. In the extreme localized case, the load is redistributed only on nearest neighbours of the broken fiber [18, 30]. Several characteristics of fracture phenomena can be investigated via fiber bundle models. A most appealing feature of FBMs is that avalanches of fiber breakings can be comfortably studied either analytically, in some cases, or by doing numerical simulations. Hansen et al. showed that the distribution of avalanche sizes in GLS model of elastic fibers follows a power-law with a universal exponent $\xi = 5/2$ for a broad class of disorder distributions [29]. In the LLS case, the distribution is also a power-law, however the exponent is significantly higher, $\xi = 9/2$ [30]. An interesting observation of Pradhan et al. was that the exponent of the avalanche size distribution shows a crossover to a lower value $\xi = 5/2 \rightarrow 3/2$ near the point of global breakdown [31, 32]. The same behaviour was found in random fuse models. This phenomenon has great relevance when monitoring the mechanical state of structural components, as the crossover of the exponent is a clearly observable sign of imminent failure.

## 2.2 Fragmentation

The breakup of a system into many pieces, i.e. fragmentation is a ubiquitous phenomenon in nature. Examples cover a huge variety of length scales ranging from the breakup of heavy nuclei through geological processes like the fragmentation of rocks to events on an astronomic scale such as supernovae. Apart from its scientific relevance, understanding fragmentation phenomena has great importance in industry since it forms the basis of processes such as comminution, crushing, milling and grain liberation [37, 38, 39, 40, 41].

Fragmentation generally occurs when a large amount of energy is suddenly imparted to a physical system resulting in the disintegration of the system into many small fragments, whose sizes are significantly smaller than the system size. The form of energy transfer can be explosion, impact on a hard wall, impact of a projectile, crushing, etc. [41, 42, 43, 44, 45, 46, 47].

### 2.2.1 Experimental results, universality in fragmentation

Before the rapid technological advances of recent decades, the only means of studying fragmentation processes was the analysis of fragment size distributions (FSDs) mainly done by sieving debris from fragmented rock samples. The most striking observation regarding size distributions is that they seem to follow a power-law behaviour with a universal exponent, i.e. an exponent independent of the amount or form of energy input or type of material. This form of fragment size distribution has been long known in the engineering and mining community as the Gates-Gaudin-Schuhmann law [48, 49, 50].

In [51, 52, 53] Turcotte, Lawn and Wilshaw gave a long enumeration of power-law exponents observed in brittle fragmentation ranging from 1.9 to 2.6. Experiments of fragmentation of volcanic pyroclasts [42, 43], liquid droplets [54, 55] and plastic materials [56] have reported smaller exponents in the range 1.1 - 1.6. Power-laws for small fragments have long been accepted as a naturally occurring common characteristic of fragmentation, suggesting, in many cases, that the process is related to critical phenomena.

### 2.2.2 Effect of dimensionality

All promising models of fragmentation, as well as overwhelming evidence from experiments suggest that universal power-law behaviour of fragment mass distributions is a common natural consequence of fragmentation processes. The power-law exponent proved to be independent of the amount of energy imparted, the form of energy transfer or type of material. The effective dimensionality of the system however plays an important role in the emerging structure of FSDs.

Fragmentation in one dimension was studied by Matsushita and Ishii [57] using thin glass rods dropped vertically onto the floor. They found the fragment size distribution to vary from log-normal to power-law with increasing impact energy. Stochastic models of one-dimensional fragmentation can be found in [58], where fracture points are chosen randomly along the rod. Power-law, exponential and log-normal size distributions can be derived depending on the a priori distribution of fracture points.

Kun et al. [59, 60] studied the explosive and impact fragmentation of closed shells. They compared experiments to simulations of a discrete element model based on the Delaunay triangulation of randomly distributed

points on a spherical surface. They found good quality agreement of power-law exponents obtained from the experiments and simulations, which proved to be slightly smaller than those found for two dimensional fragmentation experiments. They also found interesting non-trivial scaling laws regarding fragment shapes in experiments performed with egg shells and hollow glass spheres [61].

A number of experiments of impact fragmentation of brittle plates and discs [44, 45, 62] have been carried out over recent decades and a universal power-law behaviour of FSDs was always found. Figure 2.3 shows the reconstructed final states of experiments of the fragmentation of brittle plates subject to different loading conditions [44]. Oddershede et al. [46] car-

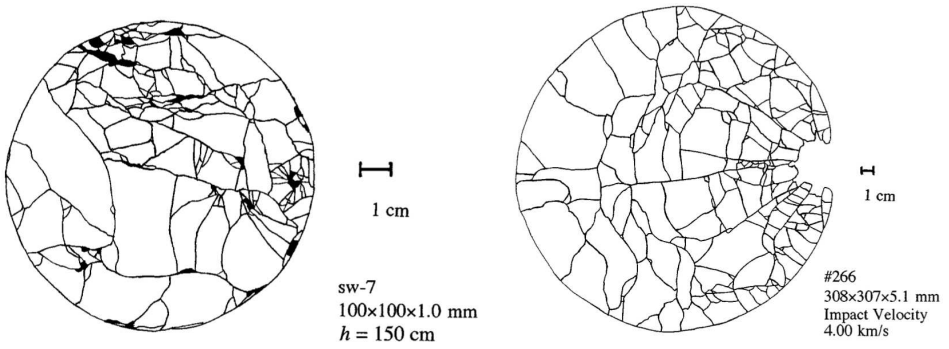


Figure 2.3: Crack patterns and fragment positions in the fragmentation experiments of Kadono et al. [44]. Circular plates of glass and plaster were fragmented in the following ways: (*left*) A glass plate trapped in a 'sandwich' configuration with a heavy iron projectile dropped on top of it. (*right*) Plaster plate fragmented by the impact of a small, high velocity projectile shot from the right.

ried out impact experiments with different types of materials with various shapes. They found that scaling exponents depend on the over-all morphology of the objects, but not on the type of material. Because of the universal power-law behaviour found without any control parameter, they concluded that fragmentation processes are self-organized critical processes with exponent $\sim 1.6$. Experiments of impact fragmentation of spheres were carried out in Refs. [63, 64, 65]. Exponents observed in the fragmentation of three-dimensional objects are slightly higher than those of two-dimensional objects.

### 2.2.3 Stochastic models of fragmentation

Over recent decades several possible mechanisms have been proposed to explain the emergence of the universal power-law behaviour. The first comprehensive study of fragment size distributions is attributed to Mott in the 1940s [66, 67, 68] where he reports experiments with fragmentation of thick shells. He compared his results with those of a one-dimensional Poisson-process and also proposed a simple two-dimensional fragmentation model: a random construction of horizontal and vertical lines dividing the plane into parts [69]. He showed that this model predicts a cumulative size distribution of the form $N(S) \sim \sqrt{S}K_1(\sqrt{S})$ where $K_1$ is a modified Bessel function. Size $S$ refers to the area of fragments. This is fairly similar to the resulting FSD of a one-dimensional Poisson-process, $N(S) \sim exp(-\sqrt{S})$.

Grady and Kipp [70] considered several models of various different constructions of lines dividing a two-dimensional plane into parts. The most realistic of these as models of fragmentation are ones that do not allow lines to intersect, representing a crack-merging scenario in solids. These models typically results in size distributions similar to that of a two-dimensional Poisson-process, $N(S) \sim exp(-S)$.

Gilvarry [71, 72] derived a form of the fragment size distribution by assuming that given a distribution of fragments, further fragmentation is determined by the uncorrelated activation of flaws within the volume, on the surface and along the edges of existing fragments. To fit experimental findings he concluded that edge flaws dominate flaw activation in explosive fragmentation. This leads to a probability density function of the form

$$n(S) \sim q(S)S^{-(d-1)/d}exp(-S/S_0) \tag{2.2}$$

where $d$ is the Euclidean dimension and $q(S)$ is the a priori density of fragment sizes. Size here means either area or volume, depending on the dimensionality of the fragments. Gilvarry chose $q(S) = V_0/S$, with which Eq. (2.2) provides excellent fits to FSDs in a great number of experiments of brittle fragmentation. The power-law exponent acquired in this case is $\gamma = (2d-1)/d$ for density functions and consequently $\gamma - 1 = (d-1)/d$ for cumulative distribution functions. In his derivation Gilvarry assumed cracks to form smooth crack surfaces, which is certainly not the case in explosive and impact fragmentation. Rapidly propagating cracks have been

shown to be unstable and as the crack accelerates beyond a critical velocity, crack branching and crack-tip splitting begin to appear. These processes have to be taken into account when dealing with fragmentation phenomena as a great number of fragments can be expected to be created by merging cracks.

Åström et al. [73, 74, 75, 76] proposed models based on this crack branching-merging scenario in two and three dimensions and derived FSDs identical to Gilvarry's result, i.e. power-law behaviour for small fragments and an exponential cutoff for large fragment sizes. They showed that the emergence of a power-law with a universal exponent $\gamma = (2d-1)/d$ can be attributed to the branching and merging tendency of rapidly propagating cracks in fragmentation processes, while an exponential cutoff for large fragments may result from the stopping of side branches due to energy dissipation. Besides the power-law they propose an additional exponential term in the FSD resulting from the Poisson process of the merging of single cracks nucleated at the beginning of the breakup process. Thus the complete form of the fragment mass distribution, as introduced in Ref. [75], is the following:

$$p(m) = \beta m^{-\alpha} e^{-\frac{m}{m_1}} + (1-\beta) e^{-\frac{m}{m_2}}, \tag{2.3}$$

where $m_1$ is the cutoff mass for fragments resulting from the branching-merging of instable cracks, while $m_2$ is the average fragment size produced by the Poisson process of merging single cracks. $\beta$ indicates the relative importance of the two mechanisms. In most cases of brittle fragmentation $\alpha$ has been shown to be close to the value $(2d-1)/d$. Figure 2.4 shows FSDs obtained in numerical simulations in Ref. [75] with various different parameter settings. All curves can be very well fitted with Eq. (2.3).

Levandovsky and Balazs [77] proposed a detailed model of crack propagation in thin brittle plates undergoing mode I fracture, based on a discretization of the continuum theory of linear elasticity. Their lattice model approach used a breaking criterion depending on the maximum eigenvalue of the strain tensor evaluated at the nodes. According to their numerical simulations fragments formed as a consequence of the merging of side branches giving rise to power-law FSDs with exponents falling in the vicinity of $(2d-1)/d = 1.5$ in two dimensions. An advantage of their model is that it allows insight into the relationship between various characteristics of brittle

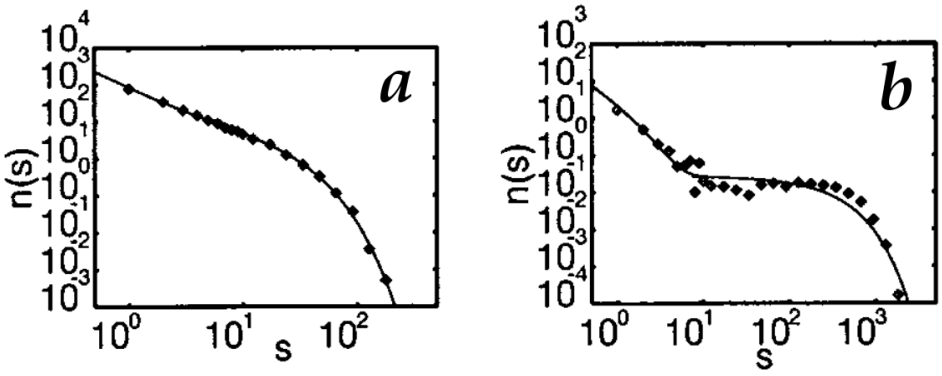


Figure 2.4: Fragment size distributions obtained in numerical simulations (see Ref. [75]). Eq. (2.3) provides an excellent fit in both cases.

fracture processes such as crack roughness, fractal dimension and fragment size distributions.

Motivated by the studies of the fractal structure of fault gouge in rocks Steacy and Sammis [78] considered an automaton model of fragmentation patterns based on the idea of preferential fracture, at all length scales, of neighbours of a particle that have the same size as the particle itself. Their results for two and three dimensions predict the emergence of random fractal fragmentation patters, with size distribution exponents falling in the range of those observed in experiments [79].

In addition to mechanism based models of fragmentation, a mean-field type approach is introduced in [80] where the time evolution of the concentration $c(x,t)$ of fragments of mass less than $x$ at time $t$ is governed by a rate equation of the form

$$\frac{\partial c(x,t)}{\partial t} = -a(x)c(x,t) + \int_x^\infty c(y,t)a(y)f(x|y)dy. \tag{2.4}$$

$a(x)$ (supposed not to depend on time) is the rate at which fragments of mass $x$ break into smaller ones and $f(x|y)$ is the conditional probability that a fragment of mass $x$ was generated from a fragment of mass $y \geq x$. Some exact solutions of Eq. (2.4) are presented in [80] with some appropriate assumptions made about $f(x|y)$, in general however solutions are very difficult to obtain. The mean field approach has successfully been applied to describe the gradual size reduction of particles in comminution devices [81],

and in granular gases [82].

Various mechanism based models provide a reasonably good explanation of the development of fragmentation patterns and the values of power-law exponents, however they lack an understanding of the complete picture in terms of dynamics, energy considerations and time evolution of fragmentation processes.

### 2.2.4 Discrete element models

Rapid advances of recent years in computational technology have made it possible to utilize very realistic Discrete Element Modelling (DEM) approaches in modeling the fracture and fragmentation of disordered materials. Molecular Dynamics (MD) simulations of DEMs have proved to be a valuable tool in studying such complicated processes [83, 84]. MD simulation methods deal with physical systems of many constituents, whose motion can be considered deterministic. The elements or particles of the system interact with each other via well defined physical laws, depending on the relevant length scale of the model. MD generates the time evolution of the system by determining the trajectories of all the particles solving Newton's equations of motion.

Two dimensional approaches are mainly based on random polygonal tesselations of the 2D plane, polygons acting as grains, with elastic beams connecting them [1]. Three dimensional models mostly focus on random close packings of spheres or other simple objects instead of space-filling constructions to save computational time [85]. Model parameters can be calibrated to various disordered solids to achieve excellent agreement in the elastic behaviour of simulated systems and real materials. Such realistic models provide access to previously unexplored details of fragmentation processes.

Here we give a typical example of a two-dimensional DEM that has been used to model disordered solids. The model was introduced long ago in Refs. [86, 87, 88], later on it was successfully applied to investigate the fracture and fragmentation of heterogeneous materials under various types of loading conditions [88, 89, 90, 91]. During my Ph.D. I used this model to study the propagation of a crack along a weak interface in such a way that I implemented the three-point bending loading condition in the simulation code of the model. Since the model can be considered as a prototype of

discrete element approaches, in the following we present the details of the model construction.

### Granularity

The granular structure of disordered solids is modeled with a vectorizable random lattice of randomly shaped convex polygons. The random configuration is obtained via Voronoi-construction [86, 87], the randomness of which can be easily varied with one parameter. The procedure is the following: We start out with a square lattice. We scatter the points necessary for the Voronoi-construction in a way, that there is exactly one point in every square. More precisely, this one point is required to lie inside a smaller square of length $a$ inside every lattice-square of unit length. This way we can control the amount of structural disorder by varying one single parameter: $a$ (Figs. 2.5, 2.6).

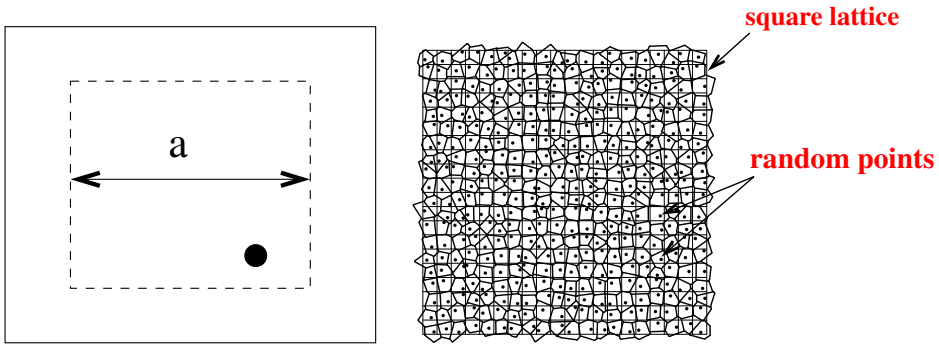


Figure 2.5: The figure on the left shows the square of unit length and in its center the square of length $a$ in which we place the initial lattice sites necessary for the Voronoi-construction. The structure of the random lattice can be seen in the figure on the right. The points used for the Voronoi-construction are marked with black dots. These dots are placed randomly and independently in the squares of length $a$ as described above.

The Voronoi method assigns a so-called Voronoi cell to each of the scattered points $P_i$, namely the set of all the points in the plane that lie closer to $P_i$ than any other point $P_j$ ($j = 1, 2, 3...N$, $j \neq i$, $N$ being the total number of scattered points). The parameter $a$ responsible for structural disorder is kept constant at a suitable value throughout all my simulations. The Voronoi cells thus generated are randomly shaped convex polygons with a relatively narrow size distribution thanks to the regularization method de-

scribed above. The polygons obtained in this way represent a larger group of atoms. These polygons - the basic elements of our simulations - interact with each other elastically. In two dimensions each polygon has three degrees of freedom: the two coordinates of the center of mass and an angle of rotation.

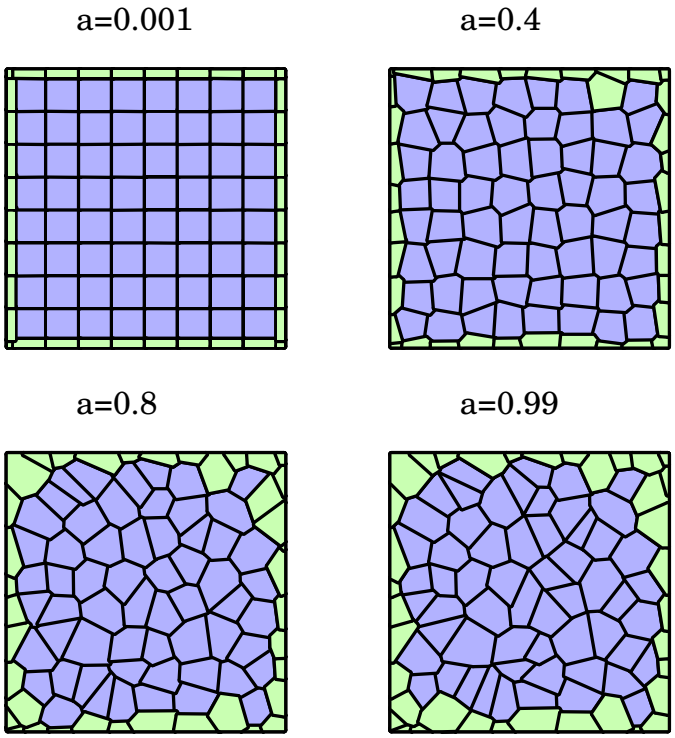


Figure 2.6: Different degrees of disorder. $a = 1$ means maximal disorder while $a = 0$ corresponds to the totally ordered square lattice.

### Elastic behaviour

Elastic behaviour in our model is achieved in the following way: the polygons symbolize rigid bodies that cannot be deformed or broken. This of course causes them to overlap when pressed against one another, and in our model, overlapping polygons exert repulsive forces on each other. Hence macroscopic deformation is made up of these small overlaps. Two overlapping polygons usually have two intersection points that define a contact-line. We define the repulsive force acting on the polygons to be proportional to

the overlap area $A$ and to be applied at the midpoint of the contact-line. The direction of the force is chosen to be perpendicular to the contact-line (Fig. 2.7).

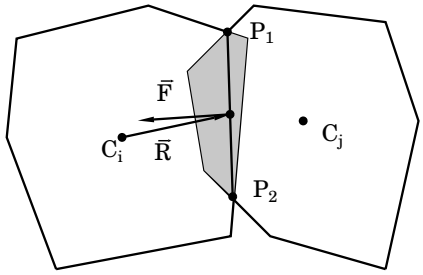


Figure 2.7: The elastic contact force caused by the overlap of two polygons. We define the contact line as the segment $P_1P_2$. The $\vec{F}$ contact force is perpendicular to the contact line and proportional to the overlap area.

The exact expression of the contact force acting between the $i^{th}$ and $j^{th}$ particles:

$$\vec{F}_{ij} = -\frac{YA}{L_c}\vec{n}, \tag{2.5}$$

where $Y$ is the grain's Young's modulus, $\vec{n}$ is the unit vector normal to the contact line and $L_c$ is the characteristic length of the given pair of polygons. This is defined in the following way:

$$\frac{1}{L_c} = \frac{1}{2(\frac{1}{r_i} + \frac{1}{r_j})}, \tag{2.6}$$

where $r_i$ and $r_j$ are the diameters of such circles that have areas equal to those of the $i^{th}$ and $j^{th}$ polygon. It is clear that the polygons generated by the Voronoi method have no overlaps, therefore there are no internal stresses present in the initial configuration. In order to form a granular solid, we also need to introduce a cohesion force between the polygons. We define beams for this purpose. We require that the center of mass of every polygon be connected by such a beam to the centers of mass of all the neighbouring polygons. These beams are elastic, they can be elongated, bent and broken. The polygons are kept together with the help of the attractive force exerted on them due to the beams' elongations. Due to the randomness of the Voronoi-construction the positions and orientations of the beams are

random. We introduce the following constants to characterize the behaviour of the beams:

$$a^{ij} = \frac{l^{ij}}{ES^{ij}}, \tag{2.7}$$

$$b^{ij} = \frac{l^{ij}}{GS^{ij}}, \tag{2.8}$$

$$c^{ij} = \frac{{l^{ij}}^3}{EI^{ij}}, \tag{2.9}$$

where $E$ and $G$ are the beam's Young's and shear modulus, $I^{ij}$ is the beam's moment of inertia with respect to shear and $S^{ij}$ is the beam's cross section area. By this we mean the length of the common side of the two polygons connected by the given beam. The beam's length $l^{ij}$ is the distance between the centers of mass of the two polygons it connects (Fig. 2.8).

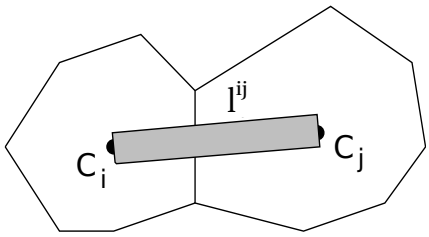


Figure 2.8: A beam connecting the centers of mass of two polygons, whose length $l^{ij}$ is the distance between the centers of mass of the polygons.

One fixed value of $E$ was used for all the polygons, while $G$ was chosen such that $b^{ij} = 2a^{ij}$ should hold. The beams' lengths, cross section areas and moments of inertia are determined by the initial arrangement of the polygons. The values of the beams' $E$ Young's moduli and the $Y$ Young's moduli of the polygons are chosen independently. In our model all the polygons have three degrees of freedom: the two components $(u_x^i, u_y^i)$ of the displacement vector of the $i^{th}$ polygon and the orientation given by a bending angle $\Theta^i$ (Fig. 2.9).

The force and torque acting on the $i^{th}$ polygon caused by the beam connecting the $i^{th}$ and $j^{th}$ positions:

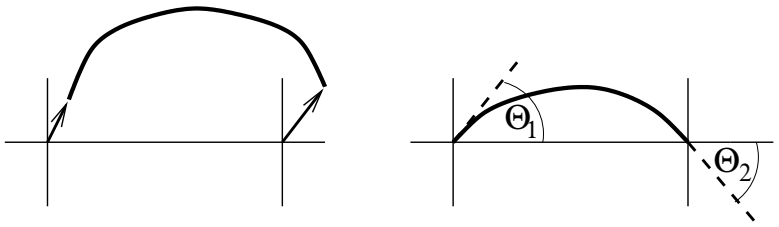


Figure 2.9: (left) The displacement vectors at the two ends of a beam connecting two lattice sites. (right) The bending angles at the two ends of the beam.

$$F_x^i = \alpha^{ij}(u_x^j - u_x^i), \tag{2.10}$$

$$F_y^i = \beta^{ij}(u_y^j - u_y^i) - \frac{\beta^{ij} l^{ij}}{2}(\Theta^i + \Theta^j), \tag{2.11}$$

$$M_z^i = \frac{\beta^{ij} l^{ij}}{2}(u_y^j - u_y^i + l^{ij}\Theta^j) + \delta^{ij} l^{ij^2}(\Theta^j - \Theta^i), \tag{2.12}$$

where $\alpha^{ij} = \frac{1}{a^{ij}}$, $\beta^{ij} = \frac{1}{b^{ij} + \frac{1}{12}c^{ij}}$ and $\delta^{ij} = \beta^{ij}(\frac{b^{ij}}{c^{ij}} + \frac{1}{3})$. This beam model is a simplified version of the Cosserat-equations of continuum elasticity [1], which is to be used to describe the elastic behaviour of granular solid materials instead of the Lamé-equation. The parameters of the beams are assigned in a way to ensure that every beam is in elastic equilibrium in the initial configuration, therefore the sample is completely stress-free in the beginning.

### Molecular Dynamics simulation

DEMs can provide a very realistic modeling approach for granular systems. The time evolution of discrete element models is generally obtained by means of Molecular Dynamics simulations, where the motion of all the elements are calculated numerically using classical mechanics. Here we provide a brief overview of MD simulation methods [83, 84, 92].

There is a variety of different algorithms for integrating systems of differential equations, with greatly varying attributes such as computational time, precision, stability [83, 92]. These have to be taken into consideration when choosing an appropriate algorithm to carry out simulations of a specific physical system. Some examples of the simplest and most time-efficient numerical integrators are the $1^{st}$-order Euler, $2^{nd}$-order Runge-Kutta, $3^{rd}$-order Verlet methods [83, 92]. When simulating systems of many particles

for many time steps however, more precise, higher order algorithms are preferred, that require only one evaluation of the interactions, the numerically most expensive operation, in each time step. A commonly used numerical integrator for MD simulations is the Predictor-Corrector method, which fulfils the requirement of precision and efficiency. We give a brief overview of the main ingredients of a $3^{rd}$-order Predictor-Corrector method based on Ref. [92]. (We consider the one-dimensional case for simplicity. Generalization to higher dimensions is straightforward.)

**Predictor-Corrector method**

As a first step one has to fix the step $\Delta t$ of the finite difference integration in terms of which the numerical solution will be tabulated. The value of $\Delta t$ should be set taking into account the characteristic time scale of the process investigated. A Predictor-Corrector method executes three operations in every iteration for every particle:
*Predictor step:* Given $x(t)$ and $v(t)$, we make a prediction of the values $x(t+\Delta t)$ and $v(t+\Delta t)$. *Evaluation step:* We evaluate the acceleration (using the defined interactions) at time $t+\Delta t$ assuming the predicted values $x(t+\Delta t)$ and $v(t+\Delta t)$. *Corrector step:* We make corrections to the predicted values $x(t+\Delta t)$ and $v(t+\Delta t)$ using the coordinates and velocity values from the previous iteration and the evaluated acceleration. The corrected values are then accepted as the numerical solution of the equation. The specific formulae for a $3^{rd}$-order Gear predictor-corrector method are given in the following [92]:
**Predictor step:** Taylor expansion of the coordinates and their derivatives truncated to obtain a closed equation system:

$$x^p(t+\Delta t) = x(t) + v(t)\Delta t + \frac{1}{2}a(t)\Delta t^2 + \frac{1}{6}b(t)\Delta t^3, \tag{2.13}$$

$$v^p(t+\Delta t) = v(t) + a(t)\Delta t + \frac{1}{2}b(t)\Delta t^2, \tag{2.14}$$

$$a^p(t+\Delta t) = a(t) + b(t)\Delta t, \tag{2.15}$$

$$b^p(t+\Delta t) = b(t). \tag{2.16}$$

**Evaluation step:**
In this step we calculate the forces and torques acting on the particles assuming the predicted values of the coordinates:

$$F^p = F(x^p, v^p) \rightarrow a^c(t + \Delta t) = \frac{F^p}{m}. \tag{2.17}$$

From $F^p$ we determine the so-called corrected acceleration $a^c(t+\Delta t)$ at time $t + \Delta t$. Note that the predicted one is given by Eq. (2.15).

**Corrector step:**

We use $a^c(t + \Delta t)$ calculated in the above step to make corrections to the predicted values. To do this we first calculate

$$\Delta a(t + \Delta t) = a^c(t + \Delta t) - a^p(t + \Delta t), \tag{2.18}$$

then make the corrections according to the following linear equations:

$$\begin{pmatrix} x^c(t+\Delta t) \\ v^c(t+\Delta t) \\ a^c(t+\Delta t) \\ b^c(t+\Delta t) \end{pmatrix} = \begin{pmatrix} x^p(t+\Delta t) \\ v^p(t+\Delta t) \\ a^p(t+\Delta t) \\ b^p(t+\Delta t) \end{pmatrix} + \begin{pmatrix} c_0 \\ c_1 \\ c_2 \\ c_3 \end{pmatrix} \Delta a(t+\Delta t).$$

The values of the constants $(c_0, c_1, c_2, c_3)$ are chosen to achieve the desired precision. For second order differential equations their values are $c_0 = 3/16$, $c_1 = 251/360$, $c_2 = 1$, $c_3 = 11/18$ [92].

**Fracture**

We defined cohesive contacts (beams) between grains (polygons) through which they can exert forces and torques on one-another. Our model thus constructed can reproduce the macroscopic elastic behaviour of solids [88]. In order to be able to simulate fracture as well, we assume our beams to have a certain rigidity with regard to deformation. By this we mean that if the elongation or bending of a beam exceeds a threshold value, then that particular beam is considered broken, it is taken out of the simulation, it no longer has any effect on the evolution of the system. Macroscopic fracture can be achieved through a series of such small microscopic fractures (Fig. 2.10).

The beams, modeling cohesive forces between grains, can be broken according to a physical breaking rule, which takes into account the stretching

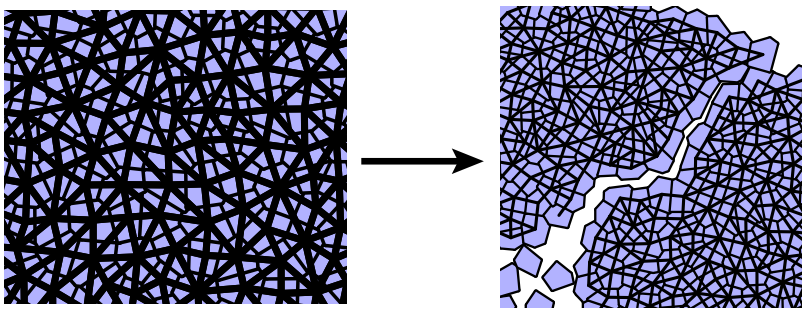

Figure 2.10: (*left*) Neighboring polygons of the initial Voronoi tessellation are connected by beams. This way a triangular beam lattice is obtained. (*right*) Due to subsequent breaking of beams a crack forms along the edge of polygons.

and bending of the connections [91, 93]

$$\left(\frac{\varepsilon}{\varepsilon_{th}}\right)^2 + \frac{max(|\Theta_1|, |\Theta_2|)}{\Theta_{th}} \geq 1. \tag{2.19}$$

Here $\varepsilon$ denotes the longitudinal deformation of a beam, while $\Theta_1$ and $\Theta_2$ are bending angles at the two beam ends (see Fig. 2.9 (right)). The breaking rule Eq. (2.19) contains two parameters $\varepsilon_{th}, \Theta_{th}$ controlling the relative importance of the stretching and bending breaking modes, respectively. The energy stored in a beam just before breaking is released in the breakage giving rise to energy dissipation. At the broken beams along the surface of the polygons cracks are generated inside the solid and as a result of the successive beam breaking the solid falls apart (see Fig. 2.10).

The time evolution of the polygonal solid is obtained by solving the equations of motion of the individual polygons. At each iteration step we evaluate the breaking criterion Eq. (2.19) and remove those beams which fulfil the condition. The simulation is continued until a relaxed state is achieved where no beams break anymore. For more details of the model construction see Refs. [88, 91].

The breaking parameters $\varepsilon_{th}$ and $\Theta_{th}$ of beams are stochastic variables in the model, i.e. they are sampled from probability density functions $p(\varepsilon_{th})$ and $p(\Theta_{th})$. The Weibull distribution provides a comprehensive description of the stochastic fracture strength of brittle materials, hence, for both threshold values the Weibull form is prescribed

$$p_{\lambda,m}(x) = \frac{m}{\lambda}\left(\frac{x}{\lambda}\right)^{m-1} e^{-(x/\lambda)^m}, \tag{2.20}$$

where $x$ denotes the two breaking thresholds $\varepsilon_{th}, \Theta_{th}$. The Weibull distribution has two parameters: $\lambda$ sets the characteristic scale of threshold values while the exponent $m$ determines the scatter of the variable. Increasing the value of the exponent $m$ the width of the Weibull distribution Eq. (2.20) decreases and converges to the delta function in the limit $m \to \infty$ (see Fig. 2.11).

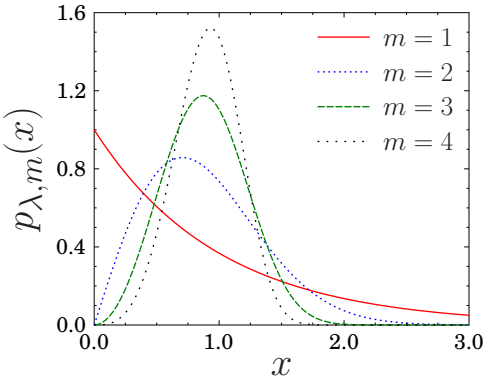


Figure 2.11: Weibull probability density functions for $\lambda = 1$, at different values of the parameter $m$.

Varying the scale parameters $\lambda_\varepsilon$ and $\lambda_\Theta$ of the breaking thresholds the relative importance of stretching and bending can be controlled in the breaking process. We note that the elastic constants of beam elements depend on the Young's modulus of beams, furthermore, also on their length and cross section. In the model the geometry of beams is determined by the Voronoi tessellation, i.e. the length and cross section of beams are defined as the distance between the centers of mass and the length of the common side of the two neighboring polygons, respectively. It has the consequence that besides the strength disorder of beams there is also structural disorder in the system determined by the initial Voronoi tessellation.

As an illustration, Fig. 2.12 presents the final stage of the breakup process of a disc-shaped solid induced by impact against a hard wall. It can be observed that around the impact site the sample is completely shattered, i.e. all the fragments are single polygons. Large fragments are formed when cracks reach the surface of the sample. For details of the simulations see

Ref. [91].

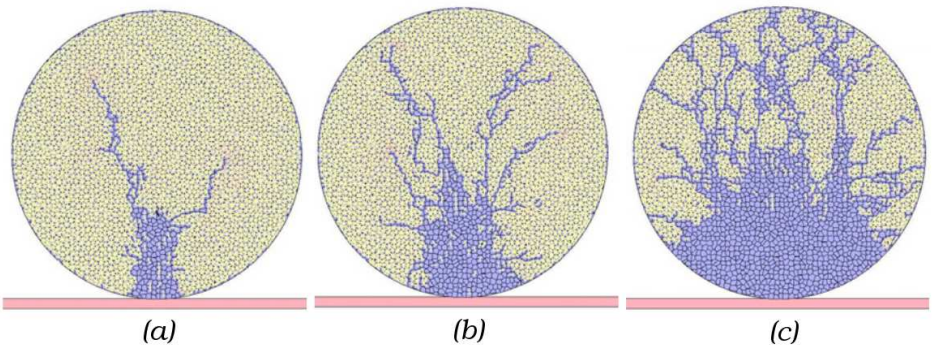


Figure 2.12: Final reassembled states of the breakup process of a disc of radius 30 $cm$ at different impact velocities dropped on a hard frictionless plate. (a) $v_0 = 100$ $cm/s$. The cone is not fully developed and only a few oblique cracks are present. (b) $v_0 = 200$ $cm/s$. More oblique cracks develop and travel a greater distance. (c) $v_0 = 600$ $cm/s$. Both oblique cracks and secondary cracks are present. (See Ref. [91].)

DEM studies of fragmentation of discs were carried out in the 1990's [90, 91] and more recently a detailed analysis of impact fragmentation of spheres was given in [85]. The simulations could reproduce experimental results to a very good approximation. A general observation in the simulations was that in every case a damaged and a fragmented state of the system could be defined as a function of the imparted energy with a rather sharp transition. For low energies the system sustains some damage but remains intact, while increasing the energy would, at some transition point $E_c$ ultimately result in a complete disintegration of the sample.

### 2.2.5 Fragmentation as a phase transition

To obtain a comprehensive understanding of the observed universality of fragmentation phenomena is the main driving force of theoretical studies. Based on discrete element simulations of the collision induced breakup of disordered solids, Kun and Herrmann [90] showed that fragmentation exhibits strong analogies to continuous phase transitions. Their simulations revealed that depending on the amount of imparted energy, the breakup process can have two substantially different outcomes: at low energy the solid only gets damaged, i.e. some microcracks nucleate, however, a big residue

survives which does not break into pieces. To achieve fragmentation the imparted energy has to surpass a threshold value $E_c$, where the power law FSD first occurs. To obtain a quantitative characterization of the damage-fragmentation transition they analyzed the moments $M_k$ of the fragment mass distributions, defined as $M_k = \sum_{i=1}^{N} m_i^k - M_{max}^k$, $m_i$ being the mass of the $i$th fragment, $N$ the total number of fragments and $k$ a non-negative integer. Careful calculations revealed that the average fragment mass, defined as $M_2/M_1$, exhibits a strong maximum at $E_c$ suggesting a possible scaling form

$$\frac{M_2}{M_1} \sim |E - E_c|^{-\gamma} \tag{2.21}$$

as seen in percolation theory [94], $\gamma$ being a critical exponent of the transition. Simulation results proved to fit Eq. (2.21) with reasonable quality, indicating $\gamma \approx 0.26$ for the fragmentation phase transition in two dimensions. They also analyzed the behaviour of the mass of the largest fragment $M_{max}$ compared to the total mass $M_{tot}$ as a function of the imparted energy, and found that $M_{max} \approx M_{tot}$ for $E < E_c$, but $M_{max}$ has a rather sharp drop near the transition point, the function $M_{max}(E)$ having a change of curvature at $E_c$. They found that the largest fragment also shows critical behaviour at $E_c$, in the form

$$\frac{M_{max}}{M_{tot}} \sim (E - E_c)^{\beta} \tag{2.22}$$

for $E < E_c$, $\beta$ being another critical exponent, $\beta \approx 0.11$ giving the best fit. This suggests that the relative mass of the largest fragment, corresponding to the strength of the infinite cluster in percolation theory [94], can be treated as the order parameter of the phase transition. The value $M_{max}/M_{tot}$ is close to unity in the damaged phase below the transition point and rather rapidly, but continuously, drops to values near zero in the fragmented phase above $E_c$, indicating that brittle fragmentation can be considered analogous to continuous phase transitions. These results suggest that the observed universality in fragmentation phenomena is the consequence of an underlying phase transition which is continuous [90].

Since then further simulations [85, 91] and experiments [55, 95, 96] have confirmed the validity of the phase transition picture of fragmentation.

Some important questions however still remain open regarding fragmentation phase transitions. How robust fragmentation universality classes are, what effect dimensionality or various material properties have on the phase transition are questions that have not been fully investigated yet.

## 2.3 Goals of research

Theoretical studies of crackling noise emerging in the fracture of heterogeneous materials have so far mostly relied on numerical simulations of simple stochastic models. The power law form of the distributions of burst sizes could be reproduced in most modelling approaches and the values of the exponents lie fairly close to those found in experiments. However, a clear understanding of how crackling noise is produced in the propagation of a single crack and the effect of the fracture process zone on the dynamics of the crack tip is still lacking. I planned to do molecular dynamics simulations of a realistic two-dimensional discrete element model to obtain a clearer picture of the mechanisms that produce crackling noise in the propagation of a single crack. To obtain a quantitative characterization of the jerky crack propagation I wanted to analyze the statistics of the jumps of the crack tip and the structure of the process zone emerging ahead of the crack tip. Details of the related research can be found in Chapter 3.

The critical nature of the fragmentation transition in brittle materials has long been recognized based on a number of experimental and theoretical studies. However, the values of critical exponents, the robustness of universality classes and the analogy to continuous phase transitions are matters of which our understanding is still rather limited. The aim of my research was to investigate the impact fragmentation phase transition of heterogeneous brittle materials by means of molecular dynamics simulations of a three-dimensional discrete element model. As a novel approach, finite size scaling analysis was planned to obtain a precise characterization of the system near the fragmentation critical point. Details of the related research can be found in Chapter 4.

The concept of universality in brittle fragmentation has been accepted for several decades. Experimental results have shown that relevant characteristics of the fragmentation process, most importantly the exponent of the fragment size distribution, depend mainly on the dimensionality of the

fragmenting system. The effect of material properties, such as plasticity, on the breakup process however is not very well known. To overcome this limitation I wanted to work out an extension of three-dimensional discrete element models capturing the effect of plasticity. Simulating the impact fragmentation of plastic spheres my goal was to clarify how plastic energy dissipation affects the outcomes of fragmentation processes. Details of the related research can be found in Chapter 5.

# Chapter 3

# Crackling noise in single crack propagation

We study the crackling noise emerging during single crack propagation in a specimen under three-point bending conditions. We carried out molecular dynamics simulations of a two-dimensional discrete element model in which the sample is discretized in terms of convex polygons and cohesive elements are represented by beams. Our simulations revealed that fracture proceeds in bursts whose size, duration and waiting time distributions have a power law functional form with an exponential cutoff. We obtained a scaling form for the characteristic quantities of crackling noise of quasi-brittle materials by varying the degree of brittleness of the sample through the amount of disorder. Our DEM approach also provides valuable insight into the spatial structure of damage, allowing us to analyze the development of a process zone in front of the crack-tip. We found that the process zone expands and shrinks in discrete steps, the sizes of which vary in a wide range. We analyzed the distribution of such steps and could also determine statistically the functional form of the damage profile in front of the propagating crack. The details of this work are published in Refs. [97, 98, 99].

## 3.1 The model

To study the dynamic fracture of disordered solids we performed Molecular Dynamics simulations [83, 84] of a realistic two-dimensional discrete element model. Considering the current speed of CPUs it would not be worth sim-

ulating in three dimensions, because the increased cost in computational time in 3D calculations would force us to settle for simulating much smaller systems. Molecular Dynamics uses Newton's equations, i.e. it calculates the motion of particles using classical mechanics. We solve the necessary differential equations using a Predictor-Corrector method. To model disordered solids we used a two-dimensional DEM, the details of which were presented in Chapter 2. The granular structure of the solid is represented by randomly shaped convex polygons that interact with each other via a repulsive overlap force. The polygons are connected by deformable elastic beams for the purpose of cohesion. These beams break if their deformation state fulfils a breaking criterion that has two breaking threshold parameters for the two possible breaking modes: $\lambda_\varepsilon$ for stretching and $\lambda_\Theta$ for bending. $\lambda_\varepsilon$ and $\lambda_\Theta$ are stochastic variables sampled from Weibull distributions.

In our study we only investigated the two limiting cases of beam breaking dominated by pure stretching or bending with the parameter settings $\lambda_\varepsilon = 0.05$, $\lambda_\Theta = 100$, or $\lambda_\varepsilon = 100$, $\lambda_\Theta = 1$, respectively. The Weibull exponents were changed in the range $1 \leq m \leq 50$ for both threshold distributions in order to control the amount of disorder in the system. For further details see Chapter 2.

**Simulation setup**

In the simulations a bar shaped specimen is considered with longer and shorter side lengths $L$ and $L_c$, respectively.

In order to make a realistic representation of three-point loading, the three loading plates are realized by additional polygonal elements, i.e. squares in Fig. 3.1 with side length $S = 5l_p$ much smaller than the longer side $L = 200l_p$ of the bar $S \ll L$. These loading plates interact with the particles of the bar via the overlap force, however, no beams are coupled to them. Strain controlled loading of the bar is implemented in such a way that the two loading plates at the bottom are fixed while the third one on the top is moved vertically downward in Fig. 3.1 with a constant speed $v_0$. The moving plate overlaps the boundary polygons on the top of the bar which results in an increasing loading force. The stiffness of the plates is set high enough to keep the overlap below 20% of the average polygon area. Simulations were carried out varying the value of $v_0$ in a range, which allows for an

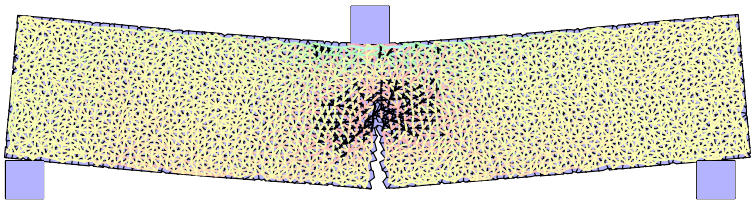

Figure 3.1: Three-point bending of a bar composed of polygonal particles. The particles are coupled by elastic beams which are colored according to the longitudinal deformation (yellow: nearly unstressed beams; red and black: elongated beams; blue and green: compressed beams). Beams are allowed to break solely along the center line of the bar. A relatively small sample is presented to have a clear view on the details of the model construction. The two loading plates at the bottom are fixed while the third one on the top moves downward.

efficient damping of the elastic waves and ensures a reasonable CPU time for the computations. The main advantage of three-point bending tests is that the highly stressed zone, where the crack appears, falls in the middle of the bar which helps to make efficient monitoring of the fracture process. In order to simplify the numerical measurements on crack propagation, we introduce a "weak" line in the middle of the bar in such a way that solely those beams are allowed to break which connect the two sides of the line (see Fig. 3.1).

## 3.2 Macroscopic response

We characterize the macroscopic mechanical response of the material in our three-point bending experiment by measuring the force $F$ acting on the moving plate at the top of the sample as a function of time $t$ (see Fig. 3.1). Our experiments are strain-controlled, the loading plate moves at a constant speed. Thus the deflection of the bar is proportional to $t$, so $F(t)$ can be considered to be the constitutive curve of the sample (Fig. 3.2). It can be observed in Fig. 3.2 (left) that the macroscopic response is linear all the way up to the peak, where the force drops suddenly. The drop becomes more drastic if we increase the brittleness of the sample by increasing the value of the Weibull exponent. In the linear part of the curve

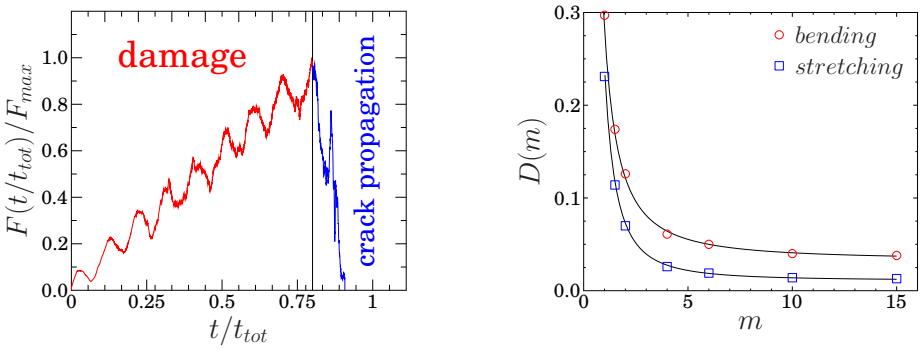


Figure 3.2: (*left*) Force $F$ normalized by the maximum value $F_{max}$ as a function of time $t$ during the loading process. Since the deflection of the bar is proportional to $t$ the curve can be considered as the constitutive curve of the sample. Oscillations occur due to elastic waves generated by the loading process. After the peak the decreasing part of $F(t)$ indicates stable crack propagation where our analysis is focused. $t_{tot}$ denotes the time of the last beam breaking. (*right*) Damage accumulated up to the peak of $F(t)$ as a function of the Weibull exponent $m$. The curves can be very well fitted with the functional form Eq. (3.1). The value of the exponent is $\mu = 1.9$ and $\mu = 1.5$ for the stretching and bending limits, respectively.

smooth oscillations about the time-average are present, which are caused by elastic waves generated by the loading plate travelling back and forth inside the sample. The period $T$ of these oscillations is approximately $T \approx 2L_c/c$, $c$ being the speed of sound inside the sample. The fact that these oscillation are so pronounced is due to the value of $v_0$ being relatively large, i.e. not negligable compared to $c$. Smaller values of $v_0$ however would make the computational time for simulations unacceptably long.

As the loading of the sample proceeds, the curve becomes more and more noisy due to microcracks nucleating throughout the breakable surface. It can be seen in Fig. 3.2 that after the maximum, the force drops down rather drastically, however the macroscopic failure is not totally abrupt. After the sharp drop, the relatively small strain rate allows for stable crack propagation where the crack gradually advances until the sample falls apart. As the bar is loaded, microcracks nucleate throughout the interface, which correspond to uncorrelated beam breaking events. This way damage is accumulated inside the sample before the onset of crack propagation. Local beam breakings inside the sample are always perfectly brittle, however the disor-

der in breaking thresholds can result in a quasibrittle macroscopic response where the constitutive curve exhibits nonlinear behaviour. It is difficult to quantify the strength of nonlinearity numerically in the $F(t)$ curve due to the disturbing effect of the oscillations. Also this nonlinearity might not be so apparent because beam breakings are limited to the weak interface. Hence we characterize the degree of brittleness of the sample and its dependence on the amount of threshold disorder by measuring the accumulated damage prior to the peak of the force as a function of the Weibull exponent $m$. We define a damage parameter $D$ as the fraction of beams broken before a single crack starts propagating. In Fig. 3.2 we present the damage parameter $D$ for the stretching and bending limits as a function of the Weibull exponent $m$. The curves can be very well fitted with the functional form

$$D(m) = B + Am^{-\mu}, \tag{3.1}$$

where the parameters $A$, $B$ and $\mu$ proved to be different for the stretching and bending limits.

The power law form of $D(m)$ can be motivated by the following simplified assumption: Let us consider a mean-field approximation of the system, where all the beams along the interface share the same $\varepsilon$ strain at any given time during the process. This way the breakable interface of the bar is substituted by a parallel bundle of beams with equal load sharing, whose breaking process can easily be described analytically [33, 34, 35]. The fraction of intact beams at any $\varepsilon$ can be given as $1 - P(\varepsilon)$ where $P(\varepsilon)$ is the cumulative probability distribution of the breaking thresholds. The macroscopic stress $\sigma$ as a function of strain $\varepsilon$ can then be written in the form

$$\sigma(\varepsilon) = [1 - P(\varepsilon)]\, E\varepsilon = e^{-(\varepsilon/\lambda)^m} E\varepsilon, \tag{3.2}$$

where $E$ is the Young's modulus of the beams. Under strain controlled loading of the bundle, stable crack propagation starts at the peak of the constitutive curve $\sigma(\varepsilon)$. After differentiating Eq. (3.2) the position of the maximum $\varepsilon_c$ reads as $\varepsilon_c = \lambda(1/m)^{1/m}$ for the Weibull distribution. The fraction of broken beams accumulated up to the peak of $\sigma(\varepsilon)$ can be obtained by plugging $\varepsilon_c$ into the cumulative distribution of thresholds $P(\varepsilon_c)$, hence, the damage parameter $D$ as a function of the Weibull exponent $m$ can be

cast into the final form for large enough $m$ values

$$D(m) \approx 1 - e^{-(1/m)} \sim m^{-1}. \tag{3.3}$$

The numerical results on the amount of damage prior to the force peak in Fig. 3.2 are consistent with the above analytic prediction. The higher value of the measured exponents $\mu^s = 1.9 \pm 0.1$ (stretching) and $\mu^b = 1.5 \pm 0.1$ (bending) is the consequence of the strain gradient in the load direction, which was completely neglected in the analytic calculations. Note that in the limit of high $m$ values, the amount of damage does not converge to zero, instead it takes a finite value $B > 0$. The non-zero value of $B$ in Eq. (3.1) can be attributed to the structural disorder in the sample, which is present and is the same for all values of the Weibull exponent. This structural disorder gives rise to fluctuations of the beam parameters which in turn result in a noisy breaking sequence in spite of the constant breaking parameters [91, 93].

Perfectly brittle failure of the bar would be characterized by a linear behavior of $F(t)$ up to the maximum without any damaging which is then followed by an abrupt breaking. Our simulation results demonstrate that varying the amount of threshold disorder we can control the degree of brittleness of the DEM sample from highly (but not perfectly) brittle to quasi-brittle. It is a very interesting question how the degree of brittleness affects the properties of crackling noise and the spatial structure of damage along the interface.

## 3.3 Crackling noise during crack propagation

Figure 3.1 shows the snapshot of our simulation of a three-point bending experiment. The colour code indicates the highly elongated state of the bottom of the specimen, where consequently the crack starts. We can observe high tensile stress concentration at the crack tip, which provides the driving force for crack propagation.

Figure 3.3 presents a better picture of the developing stress field inside the sample when the propagating crack is half-way along the cross-section of the specimen. This map was constructed by applying a moving average over the stress state of the beams and averaging over 100 simulations with varying initial geometry. One clearly sees the high stress concentration around the

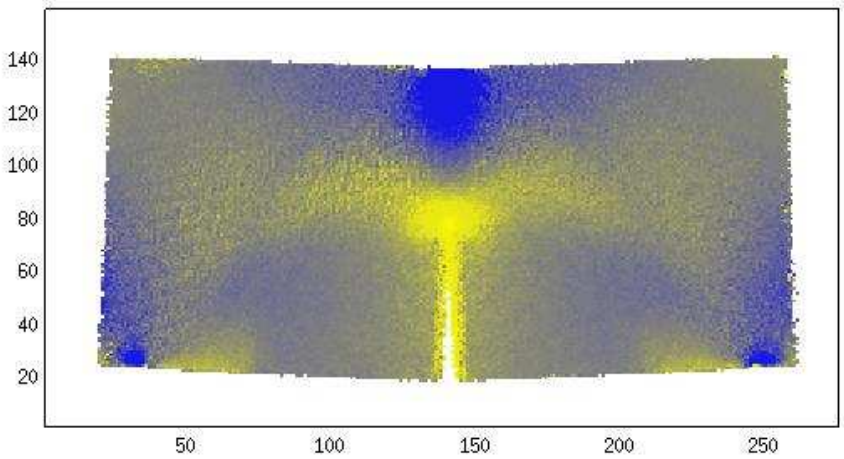


Figure 3.3: Tensile stress field inside the sample with the propagating crack halfway along the cross-section. Grey corresponds to unstressed regions, while yellow refers to tensile and blue to compressive stress. The tensile stress concentration around the crack-tip is clearly visible.

crack tip and also the high compressive stress arising near the loading plate and the two holding plates at the bottom. Stress relaxation along the crack surface is also visible. The constant speed of the loading plate ensures a strain-controlled loading of the specimen at a fixed strain rate. Due to the low value of the loading speed at most one beam breaks in one iteration step of the MD simulation. After a local breaking event the stress gets redistributed, increasing the stress concentration on the intact beams ahead of the crack. This may give rise to additional breakings, resulting in a correlated trail of breaking events.

In order to identify bursts of local breakings we introduce a correlation time $t_{corr}$: if the time difference of two consecutive beam breakings occurring at times $t_i$ and $t_{i+1}$ is smaller than the correlation time $t_{i+1} - t_i < t_{corr}$ the two breakings are considered to belong to the same burst. The value of the correlation time was chosen in such a way that it is larger than the time step $\Delta t$ used in the integration of the equation of motion but it is much smaller than the total duration $t_{tot}$ of the breaking process, i.e. we set $t_{corr} = 10\Delta t$ for which $10^5 t_{corr} < t_{tot}$ holds. The size of bursts $\Delta$ is defined as the number of beams breaking during the correlated sequence. When the amount of disorder is very high $m \to 1$, especially in the bending limit of breakings, it may happen in DEM simulations that very distant beams break within

the correlation time, however, without any correlation. To obtain information on the strength of spatial correlations in an avalanche, we calculate the distance $h_j = |y_j - y_{j+1}|$ between consecutive beam breakings with the positions $y_j$ and $y_{j+1}$ and sum it up inside an avalanche $h = \sum_{j=1}^{\Delta-1} h_j$. For a strongly correlated avalanche where each consecutive breaking occurs on adjacent beams the ratio of $h$ and of the burst size $\Delta$ is close to the characteristic polygon size $h/\Delta \approx l_p$. In order to filter out avalanches dominated by random coincidences we introduce a threshold value for this ratio, i.e. those avalanches for which $h/\Delta > 2l_p$ holds are removed from the statistics. Computer simulations showed that in the stretching limit the above condition has no effect, however, in the bending limit where a high amount of distributed cracking occurs, about 10% of the avalanches are filtered out due to random coincidences (compare also to Fig. 3.2 (right)).

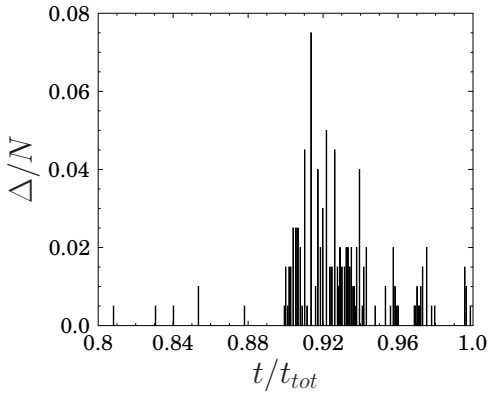


Figure 3.4: Time series of bursts in a single fracture simulation. The bursts are correlated breaking sequences of beams which then result in sudden jumps of the extending crack. $N$ denotes the total number of beams along the weak interface where the crack propagates. For all the simulations its value was set to $N = 200$. At the beginning of the loading process, for a considerable time no breaking occurs, most of the breaking events appear at larger deflections beyond the peak of the constitutive curve (see Fig. 3.2). Hence, we magnify the final section of the bending process.

In Figure 3.4 we present a time series of bursts in a single fracture simulation, the length of vertical lines representing the size of the bursts calculated in the manner defined above. Bursts are visibly separated by silent periods of greatly varying length. These waiting times correspond to the durations

of states of the system where the crack tip is pinned due to the presence of some strong beams. At the beginning of the loading process the bursts are small compared to the cross section of the specimen, with increasing deflection of the bar however, bursts become larger and their size $\Delta$ tipically reaches a maximum somewhat before the onset of macroscopic failure. After the maximum, as the crack approaches the top of the bar, burst sizes decrease while waiting times increase indicating a slowing down of the crack.

We determined numerically the size distribution of bursts $P(\Delta)$ varying the amount of disorder in the breaking thresholds. The size distributions for different values of the Weibull exponent for the absolute stretching and bending limits are presented in the insets on the left and right hand sides of Fig. 3.5 respectively. It can be observed that increasing the Weibull exponent $m$, i.e. decreasing the amount of disorder, the bursts get larger but the functional form of the distributions does not change.

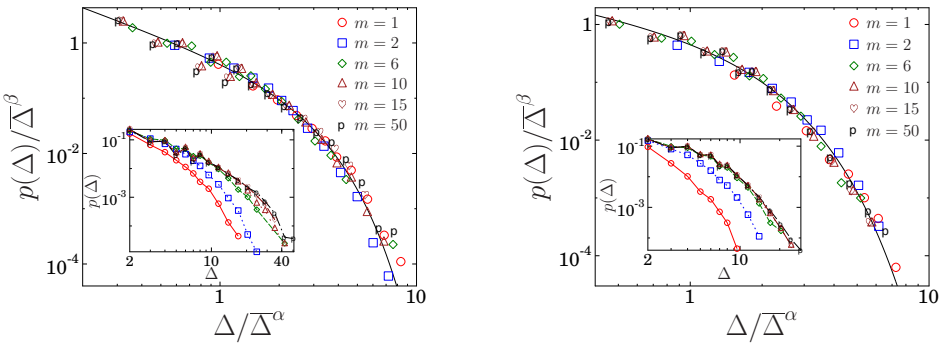


Figure 3.5: (*left*) Inset: Avalanche size distributions for the absolute stretching limit varying the value of the Weibull exponent $m$. The main panel presents the excellent data collapse obtained by rescaling the distributions with the average burst size according to Eq. (3.4). Scaling exponents: $\alpha^s_\Delta = 1.4 \pm 0.5, \beta^s_\Delta = 1.8 \pm 1$. The parameter values obtained by fitting Eq. (3.5) are $a^s_\Delta = 0.55, \tau^s_\Delta = 1.3 \pm 0.2, b^s_\Delta = 2.2, \delta^s_\Delta = 1.5 \pm 0.3$. (*right*) Inset: avalanche size distributions for the absolute bending limit. The main panel shows that rescaling the distributions according to Eq. (3.4) an excellent data collapse is obtained. Scaling exponents: $\alpha^b_\Delta = 1.4 \pm 0.5, \beta^b_\Delta = 1.8 \pm 1$. The fit parameters of the scaling function are $a^b_\Delta = 0.85, \tau^b_\Delta = 0.8 \pm 0.3, b^b_\Delta = 1.4, \delta^b_\Delta = 1.3 \pm 0.3$.

For small bursts a power-law behaviour is obtained followed by a rapidly decreasing cutoff regime. The main panels in Fig. 3.5 demonstrate that the

burst size distributions $P(\Delta)$ obtained at different $m$ values can be made to collapse onto a master curve by using the average burst size $\overline{\Delta}$ as a scaling variable. The data collapse implies the scaling structure

$$P(\Delta) = \overline{\Delta}^{\beta} f(\Delta/\overline{\Delta}^{\alpha}), \tag{3.4}$$

where the values of the exponents were determined numerically $\alpha^s_\Delta = 1.4 \pm 0.5$, $\beta^s_\Delta = 1.8 \pm 1$, and $\alpha^b_\Delta = 1.4 \pm 0.5$, $\beta^b_\Delta = 1.8 \pm 1$ which provide the best quality collapse for stretching and bending, respectively. The scaling function $f$ can be very well fitted by the form

$$f(x) = a x^{-\tau} e^{-(x/b)^{\delta}}, \tag{3.5}$$

where the parameter values providing the best fit are $a^s_\Delta = 0.55, \tau^s_\Delta = 1.3 \pm 0.2, b^s_\Delta = 2.2, \delta^s_\Delta = 1.5 \pm 0.3$ (stretching), and $a^b_\Delta = 0.85, \tau^b_\Delta = 0.8 \pm 0.1, b^b_\Delta = 1.4, \delta^b_\Delta = 1.3 \pm 0.3$ (bending).

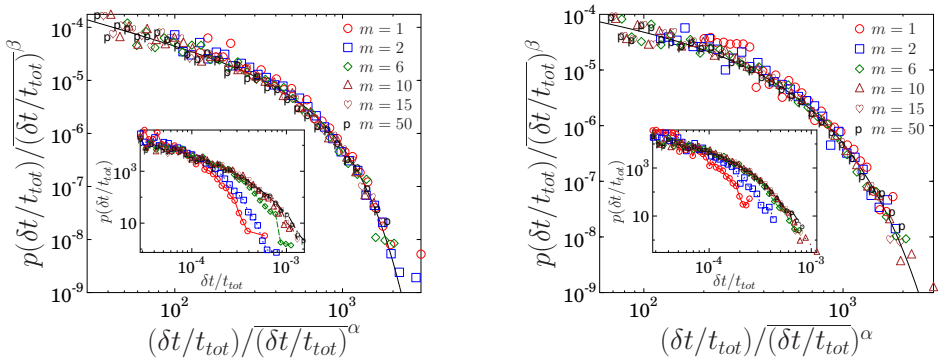


Figure 3.6: (*left*) Inset: Avalanche duration distributions for the absolute stretching limit varying the value of the Weibull exponent $m$. The main panel presents the excellent data collapse obtained by rescaling the distributions with the average burst duration according to Eq. (3.4). Scaling exponents: $\alpha^s_{\delta t} = 1.6 \pm 0.5, \beta^s_{\delta t} = 2.1 \pm 1$. The parameter values obtained by fitting Eq. (3.5) are $a^s_{\delta t} = 0.003, \tau^s_{\delta t} = 0.9 \pm 0.15, b^s_{\delta t} = 560, \delta^s_{\delta t} = 1.5 \pm 0.3$. (*right*) Inset: Avalanche duration distributions for the absolute bending limit. The main panel shows that rescaling the distributions according to Eq. (3.4) an excellent data collapse is obtained. Scaling exponents: $\alpha^b_{\delta t} = 1.6 \pm 0.5, \beta^b_{\delta t} = 2.1 \pm 1$. The fit parameters of the scaling function are $a^b_{\delta t} = 0.001, \tau^b_{\delta t} = 0.6 \pm 0.1, b^b_{\delta t} = 320, \delta^b_{\delta t} = 1.1 \pm 0.2$.

Another quantity that characterizes the magnitude of bursts is their duration, defined simply as the difference in time of the last and the first breaking event in one particular burst. The distributions of burst durations have been determined numerically for the same set of Weibull exponents as earlier in both the stretching and bending limit (Fig. 3.6).

Duration distributions proved to have the same scaling structure as the size distributions (Eq. (3.4)), with the form Eq. (3.5) once again being a very good approximation of the scaling function. The values of the scaling exponents are $\alpha^s_{\delta t} = 1.6 \pm 0.5$, $\beta^s_{\delta t} = 2.1 \pm 1$, and $\alpha^b_{\delta t} = 1.6 \pm 0.5$, $\beta^b_{\delta t} = 2.1 \pm 1$ for stretching and bending respectively. The parameter values giving the best fit of the scaling function are $a^s_{\delta t} = 0.003, \tau^s_{\delta t} = 0.9 \pm 0.15, b^s_{\delta t} = 560, \delta^s_{\delta t} = 1.5 \pm 0.3$ (stretching), and $a^b_{\delta t} = 0.001, \tau^b_{\delta t} = 0.6 \pm 0.1, b^b_{\delta t} = 320, \delta^b_{\delta t} = 1.1 \pm 0.2$ (bending). It is not surprising that the functional form and scaling behaviour of duration distributions is so similar to those of size distributions, both being quantities characterizing the magnitude of bursts. The exponents $\tau^s_{\delta t}$ and $\tau^b_{\delta t}$ of duration distributions however tend to be smaller than those of the corresponding size distributions ($\tau^s_\Delta$ and $\tau^b_\Delta$).

These results demonstrate that the growth of a crack in a disordered medium is not a smooth process. Slow driving results in a jerky crack propagation composed of a large number of discrete steps. The growth steps are sudden bursts of breakings with variable size and duration. The correlation of consecutive local beam breakings leads to a power-law functional form of the size and duration distributions with exponential cutoffs. Our most striking result is that the amount of disorder affects only the characteristic scale of bursts but the functional form and the value of the power law exponents remain the same. It is also interesting to note that the power-law exponents corresponding to stretching- and bending-dominated breaking are significantly different (beyond error bars). The functional form Eq. (3.5) has also been found to provide a good quality description of the amplitude distribution of acoustic bursts in three-point bending experiments on concrete samples [23, 100].

It can be observed in Fig. 3.4 that the bursts are separated by silent periods where no beam breaking occurs. The system relaxes slightly after every burst and is able to withstand a further increase of strain as the loading plate gradually advances. After some waiting time $T$ however the crack is

reactivated in the form of another burst. It can be seen in Fig. 3.4 that the duration $T$ of these waiting times varies in a broad range.

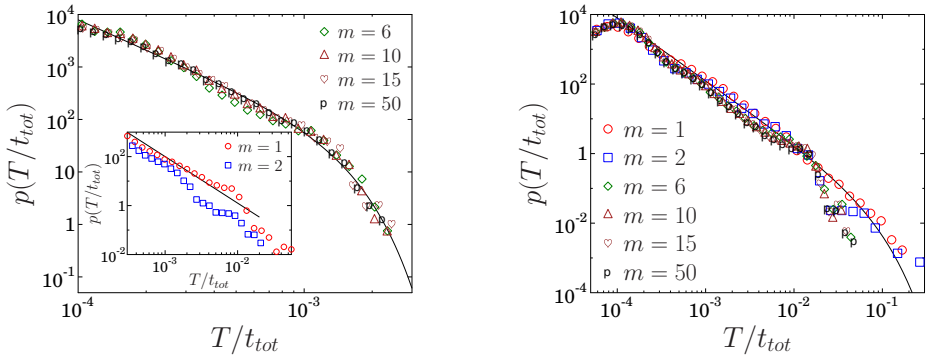


Figure 3.7: (*left*) Waiting time distributions for absolute stretching. The main panel presents curves for low disorder, where the fit was obtained with the exponent $\tau_T^s = 1.9 \pm 0.15$. The inset shows the corresponding curves for high disorder, where a crossover is obtained to a lower exponent $\tau_T^s = 1.5 \pm 0.1$. (*right*) Waiting time distributions for the absolute bending limit. The amount of disorder only affects the cutoff but the exponent is constant $\tau_T^b = 1.8 \pm 0.15$.

Waiting time distributions $P(T)$ are presented in Fig. 3.7 for the stretching limit separated for high (inset) and low disorder (main panel). For low enough disorder (main panel of Fig. 3.7) the waiting time distributions were found to be the same, showing no dependence on the Weibull exponent. The functional form of $P(T)$ can be well fitted by the expression [Eq. (3.5)] where the value of the exponent $\tau_T^s = 1.9 \pm 0.15$ was obtained. The relatively high value of $\tau_T^s$ implies that long waiting times are very rare in the trail of bursts when the material is very brittle. However, in the limit of high disorder $m \to 1$ (inset of Fig. 3.7) waiting times span a broader range and reach an order of magnitude larger values than for the very brittle materials with low disorder. The most remarkable feature of waiting time distributions is that increasing the disorder the exponent of the power law regime changes to the lower value $\tau_T^s = 1.5$ coinciding with the recurrence time exponent of one-dimensional random walks. In the absolute bending limit (see Fig. 3.7) $P(T)$ has qualitatively the same behavior as in the stretching limit. Due to the fragility of the system at all Weibull exponents $m$, the change of disorder only results in a change of the cutoff, however, the value of the exponent of

the power law regime remains constant $\tau_T^b = 1.8 \pm 0.15$.

## 3.4 Spatial structure of damage

As discussed earlier, at the time of the sudden drop of the force a crack initiates at the bottom of the breakable interface of the sample and proceeds in a jerky manner. Crackling noise analyzed in the previous section characterizes the temporal fluctuations of the advancing crack. Our discrete element modeling approach allows us to investigate the spatial structure of damage as well. In our simulations we identify a crack as a continuous region of broken beams starting from the bottom of the interface, as demonstrated in Figure 3.8. Due to the high stress concentration ahead of the crack tip and the quenched disorder of the local strength of beams, we observe the emergence of a sequence of broken and intact beams in front of the crack followed by a continuous region of intact elements reaching to the top of the interface.

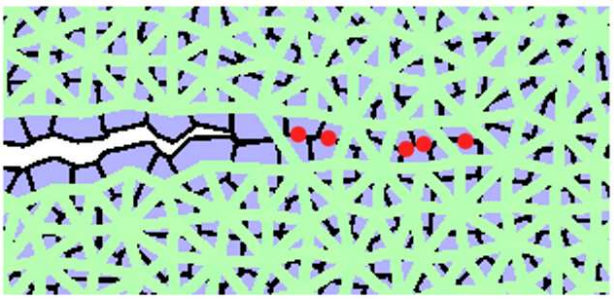

Figure 3.8: Crack tip and the process zone in front of it. Red dots indicate the positions of broken beams. The process zone is identified as a sequence of broken and intact beams starting at the crack tip and ending at the start of the continuous sequence of intact fibers.

In our model the position of the crack tip can be precisely defined as the position of the first intact beam starting from the bottom of the specimen. The sparse region of broken and intact beams between the crack tip and the last broken contact, can be identified as the fracture process zone (FPZ) whose dynamics has a strong influence on the time evolution of the breaking process [101]. It is important to note that before the crack starts propagating there is already an initial background damage $D$ present in the sample in

the form of uncorrelated breakings of weak beams (see Fig. 3.2). This also affects the extension of the process zone. The higher amount of background damage in the bending limit results in a larger extension of the process zone than for the case of stretching dominated breaking.

### 3.4.1 Dynamics of the process zone

Crack propagation is strongly determined by the dynamics of the process zone. As a beam in front of the crack breaks, a sudden discrete change in the extension of the process zone occurs. When there is a beam breaking (microcrack nucleating) inside the intact zone the FPZ extends by a length $l_{nucl}$ called the nucleation length. $l_{nucl}$ is simply the distance between the beginning of the intact zone (prior to the last breaking) and the position of the most recently broken beam. When the beam at the crack tip breaks, we witness a shrinkage of the process zone which corresponds to a jump of the crack tip (CTJ) by a distance $l_{CTJ}$, which is the distance between the position of the crack tip before and after the beam breaking. The notion of crack tip jump lengths has also recently been introduced in the framework of Quantized Fracture Mechanics [102, 103, 104]. If there is a beam breaking inside the process zone than the extension of the FPZ remains the same.

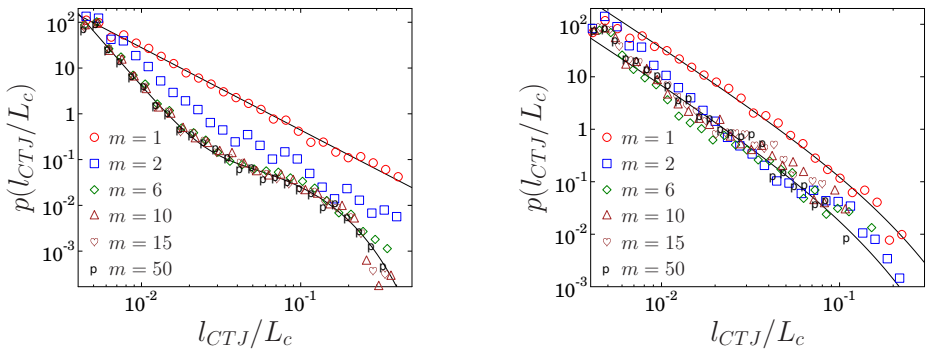


Figure 3.9: (*left*) Crack tip jump length distributions for the absolute bending limit. The values of the exponent $\gamma^b$ of the fitted curves are 1.8 and 4. (*right*) Crack tip jump length distributions for the absolute stretching limit. The value of the exponent of the power law regime is $\gamma^s = 2.2 \pm 0.1$, it does not depend on the amount of disorder.

In order to characterize the dynamics of the process zone we investigate

the probability distribution of nucleation lengths $p(l_{nucl})$ and the lengths of crack tip jumps $p(l_{CTJ})$. Fig. 3.9 shows that for low disorder (high Weibull exponent $m$) in the bending limit of breakings the distribution of crack tip jumps has a power law decay in the regime of small $l_{CTJ}$ values which is complemented by an exponential form for large $l_{CTJ}$

$$p(l_{CTJ}) = a l_{CTJ}^{-\gamma} + c e^{-l_{CTJ}/b}. \tag{3.6}$$

The additive coupling of the two terms of Eq. (3.6) shows that different mechanisms are responsible for generating small and large crack tip jumps. The small ones are determined by the stress concentration at the crack tip and by the resulting correlation of local breakings.

The Poisson-like behaviour of large crack tip jumps however originates from the randomness of the rather large initial jump-in of the crack at the onset of crack propagation. The value of the exponent $\gamma^b$ changes from $\gamma^b = 1.8 \pm 0.1$ to $\gamma^b = 4 \pm 0.2$ as the amount of disorder decreases. In the stretching limit of breakings the sample behaves in a less fragile way, less background damage is accumulated before the onset of crack propagation (see also Fig. 3.2), significantly decreasing the length of the initial jump-in. Hence, the additive exponential term does not occur in the probability distributions of the stretching limit (Fig. 3.9). The functional form of the distributions in this case is purely a power-law with an exponential cutoff. The value of the exponent $\gamma^s = 2.2 \pm 0.1$ does not depend on the amount of disorder and it falls between that of the low- and high-disorder limits of the bending limit.

The statistics of crack tip jumps was acquired throughout the intire crack propagation process. When collecting nucleation length data, we only analyzed microcracks occurring ahead of the crack tip at the time when the crack is approximately half-way across the interface.

Figure 3.10 shows the distribution $p(l_{nucl})$ for the bending limit for various values of the Weibull exponent. A power-law form is obtained for low length values

$$p(l_{nucl}) \sim l_{nucl}^{-\kappa} \tag{3.7}$$

with an exponent $\kappa^b = 1.8 \pm 0.15$. The form of the distribution functions

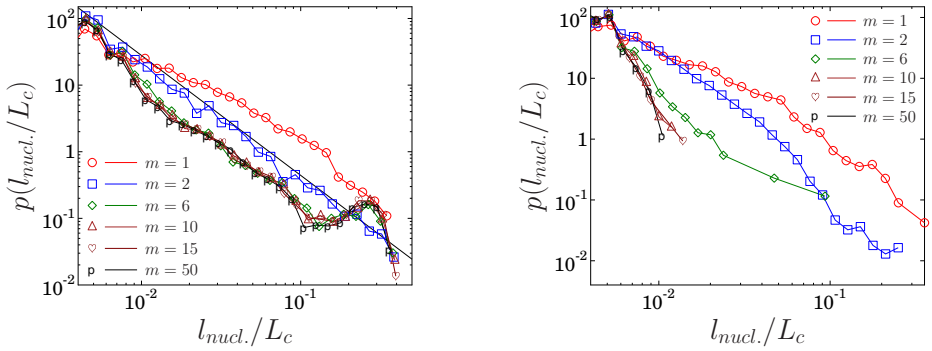


Figure 3.10: (*left*) Nucleation length distributions for the absolute bending limit varying the Weibull exponent $m$. The amount of disorder does not have a relevant effect on the distribution. The exponent of the fitted power law is $\kappa^b = 1.8$. (*right*) Nucleation length distributions for the absolute stretching limit. Decreasing disorder leads to localization of damage at the crack tip.

is not affected greatly by the amount of disorder, and for low disorder it doesn't show dependence on $m$ at all.

The situation is very different in the case when breakings are dominated by tensile stresses (Fig. 3.9). At high disorder the form of the distributions is similar to those of the bending limit with nucleation length values spanning approximately two orders of magnitude. The presence of very weak beams in these cases permits nucleation lengths of up to 40% of the cross section of the specimen. At low disorder however the nucleation of new microcracks is localized to the close vicinity of the crack tip and the largest nucleation lengths reach only about $1\% - 2\%$ percent of the cross section. These results on the distance to new nucleations and the length of crack tip jumps clearly demonstrate that in the case of bending dominated breaking varying the amount of disorder does not have a strong effect on the spatial distribution of damage. The dynamics of the process zone is mainly determined by the long range redistribution of stresses arising from the bending distorsion. However, when breaking is dominated by tensile deformation, disorder plays a crucial role in the evolution of the fracture process zone, i.e. at low disorder the process zone expands in a large number of small steps while shrinking occurs in the form of a few larger jumps. When the disorder is high, both shrinking and expanding steps can span a broad range.

### 3.4.2 Damage profile

To analyze quantitatively the extension and the structure of the process zone, we calculated the spatial distribution of damage in front of the crack tip when the crack spans half of the specimen's cross section. Fig. 3.11 presents the damage $d$, i.e. the probability of beam breaking as a function of the distance $r$ measured from the crack tip for the stretching limit of the model.

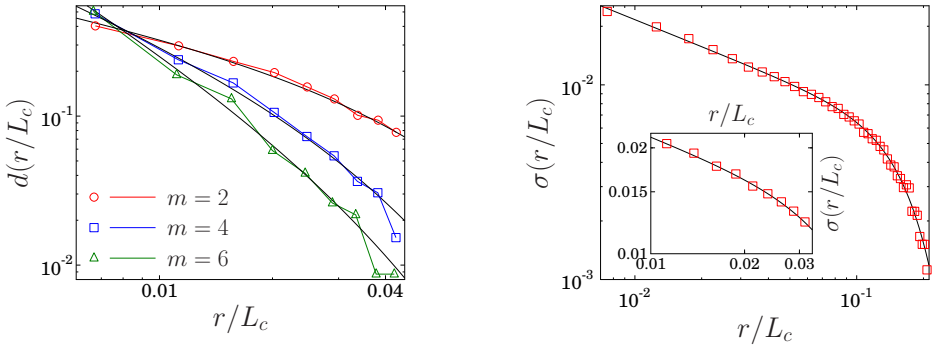


Figure 3.11: (*left*) Damage profile for different values of the Weibull exponent $m$. The distance $r$ measured from the crack tip is normalized by the cross section $L_c$ of the specimen. The values of the fitting parameters are: $\rho = 0.5$, $r_0 = 0.05$ ($m = 2$), $\rho = 1.0$, $r_0 = 0.035$ ($m = 4$), $\rho = 1.5$, $r_0 = 0.033$ ($m = 6$). (*right*) Main panel: average tensile stress as a function of the distance from the crack tip. The form of the function can be very well approximated by Eq. (3.12) with the power-law exponent $\omega = 0.46$. The inset shows the stress decay with a slightly better resolution for shorter distance. The best fit here is provided by $\omega = 0.35$.

The numerical results clearly demonstrate the fact that larger Weibull exponents, i.e. higher degree of brittleness results in smaller process zones. For all Weibull exponents the curves can be well described by a power law functional form with an exponential cutoff

$$d(r) \sim r^{-\rho} \exp\left(r/r_0\right), \tag{3.8}$$

where the extension of the process zone can be characterized by the length $r_0$. It can be observed in Fig. 3.11 that both the exponent $\rho$ and the characteristic length $r_0$ depend on the amount of disorder $m$. Fitting the

formula Eq. (3.8) to the simulated data we obtained the following parameter values: $\rho = 0.5$, $r_0 = 0.05$ ($m = 2$), $\rho = 1.0$, $r_0 = 0.035$ ($m = 4$), $\rho = 1.5$, $r_0 = 0.033$ ($m = 6$).

In order to obtain an analytic understanding of the functional form of the damage profile $d(r)$ we can start from the result of fracture mechanics that in the vicinity of the crack tip the stress has a power law decay

$$\sigma(r) = ar^{-\omega}. \tag{3.9}$$

For the exponent $\omega$ linear fracture mechanics predicts the value $\omega = 1/2$ [101], while fractal cracks and plastic or hyper-elastic constitutive laws lead to different values of $\omega$ [105].

Hence, the probability of beam breaking as a function of $r$ can be estimated as

$$d(r) = P(\sigma(r)), \tag{3.10}$$

where $P(x)$ is the cumulative distribution function of the breaking thresholds. Since our breaking thresholds are Weibull distributed, we have $d(r) = 1-e^{-(\sigma(r)/\lambda)^m} = 1-e^{-(br^{-\omega m})}$ where $b = (a/\lambda)^m$. Restricting the calculation for small distance we arrive at the form

$$d(r) \approx br^{-\omega m}. \tag{3.11}$$

The curves of Eq. (3.8) in Fig. 3.11 are consistent with the analytical expression Eq. (3.11) for low values of $r$.

Comparing the results to Eq. (3.8) the exponent $\rho$ obtained by fitting the numerical data can be written as a product of the exponents of stress decay and disorder $\rho = \omega m$. Substituting the numerical values of $\rho$ and the Weibull exponents $m$ the exponent $\omega$ describing the decay of the stress field can be determined as $\omega \approx 0.25$ for all $m$ values. The independence of $\omega$ from the disorder shows the consistency of our results. Also this value of the stress decay exponent falls rather close to the analytic result of $\omega = 1/2$ of linear fracture mechanics [101].

In our DEM approach we can numerically calculate the form of the tensile stress decay function by applying a moving average smoothing over the stress state of beams in the vicinity of the crack tip and averaging over 100 simulations. The averaging was done in all cases when the crack tip was exactly half-way along the interface. Figure 3.11 (right hand side, main panel) demonstrates that the stress decay in our simulations can be well fitted with the form

$$\sigma(r) \sim (r)^{-\omega} e^{-(r/r_0)^{\vartheta}} \tag{3.12}$$

with the values $\omega = 0.46$, $\vartheta = 3$. A curve with a finer resolution of the stress decay for shorter distance however (Fig. 3.11 right hand side, inset) gives a slightly smaller exponent $\omega = 0.35$. This is quite close to the value $\omega = 0.25$ we obtained from our calculations of the damage profile. These low values of the exponent probably arise from the shielding effect of the microcracks in front of the crack tip. In our case this shielding of the stress field is only a weak effect due to the fact that microcracks can only nucleate along the interface. If we were to allow breakings anywhere in the two-dimensional plane, presumably the shielding would be more drastic, resulting in a purely exponential damage profile, as reported in [28, 106]. Our results clearly demonstrate that the amount of disorder can have a strong effect both on the shape and extension of the process zone.

### 3.4.3 Conclusions

We investigated the properties of crackling noise emerging during the jerky propagation of a crack in three-point bending tests using a discrete element modeling technique. Our two-dimensional DEM approach provides a realistic representation of the microstructure of the material, the formation of microcracks, and the emerging complicated stress field naturally accounting for the correlation of microfractures. We proposed a numerical technique to identify avalanches based on the temporal and spatial correlation of microfractures [97, 98, 99].

We showed that for quasi-brittle materials the size of bursts and the waiting times between consecutive events are characterized by power law functional forms with an exponential cutoff. The numerical value of the

exponents have a reasonable agreement with recent experimental findings on crackling noise in three-point bending tests on concrete specimens [23, 100, 107, 108, 109, 110, 111]. This agreement also demonstrates the importance of spatial correlations of consecutive microfractures in the emergence of crackling noise.

An important advantage of our DEM approach is that it provides direct access to the spatial structure of damage. Simulations revealed that ahead of the crack tip a process zone develops which is a sparse region of broken and intact elements. The fracture process zone proved to play an important role in the advancement of the crack: on the one hand the crack progresses by shrinking and expanding steps of the zone, on the other hand, micro-cracks can shield the stress field around the crack tip which helps to stabilize the system. Recently the spatial structure of damage has been analyzed in the framework of the fuse model [28, 106]. Quasistatic loading simulations were performed starting with a notch in the middle of the fuse lattice analyzing the damage structure in the vicinity of the crack tip just before macroscopic breakdown. It was found that the damage profile has an exponential decay along the line of the crack and the characteristic length scale of the exponential was suggested as the extension of the process zone. Since linear fracture mechanics predicts a power law decay of the stress to the background level ahead of the crack tip, the authors argued that the cloud of microcracks shields the crack tip giving rise to an exponential decay. In our system at short distances a power law decay of the damage profile was obtained which is followed by an exponential cutoff. We think the power law functional form prevails in our system for the damage profile because microcrack nucleation cannot occur in the two-dimensional plane but it is restricted to a "weak line" in the sample which decreases the effect of shielding. This shielding, however, is responsible for the lower exponent of the stress decay $\omega$ and for the exponential cutoff of the damage profile. Computer simulation are complemented by analytic calculations under simplifying conditions, which provided a reasonable agreement with the numerical results [97].

# Chapter 4

# Scaling in impact fragmentation

We investigate the impact fragmentation of spherical solid bodies made of heterogeneous brittle materials by means of a three- dimensional discrete element model [112]. Our primary aim was to obtain a better understanding of the damage-fragmentation transition which has been shown to share numerous similarities with continuous phase transitions. We carried out molecular dynamics simulations and performed a finite size scaling analysis to determine the critical exponents of the phase transition and deduce scaling relations in terms of the size $R$ and impact velocity $v_0$. Our analysis proved that the exponent of the fragment mass distribution is independent of the impact velocity. We studied the dependence of the characteristic time scale of the breakup process on the impact velocity and found a novel scaling behavior in the fragmented regime which is substantially different from its two-dimensional counterpart.

## 4.1 The model

We have been using a Discrete Element Model (DEM) to carry out molecular dynamics simulations of the fragmentation of a spherical body due to impact on a hard wall. The model was introduced in Ref. [85] and it has been successfully applied to study the impact fragmentation of brittle spheres [85]. The spherical sample is represented as a random packing of spheres with a bimodal size distribution (Fig. 4.1), i.e. a one-to-one mixture of

spheres of two different sizes is generated to avoid artificial ordering.

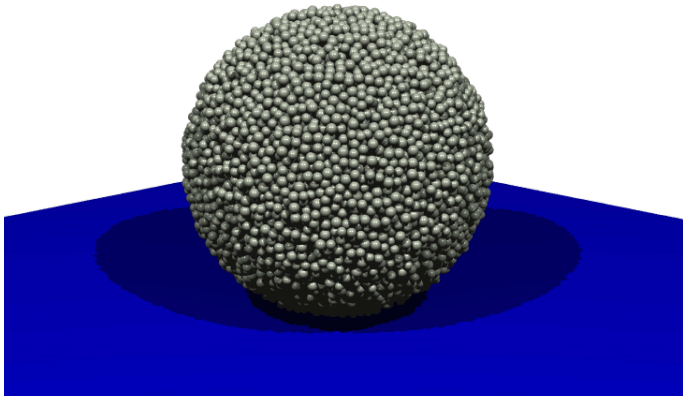

Figure 4.1: Spherical DEM sample impacting on a hard plate. The sample is made up of a random close packing of 22013 small spherical particles.

The interaction of particles is defined such that the model correctly reproduces the macroscopic constitutive behaviour of linearly elastic materials. To capture fracture and fragmentation of the solid, the interparticle contacts break when they get overstressed according to a physical breaking rule. Details of the model construction have recently been presented in Ref. [85], here we provide a short summary of the main ingredients.

### 4.1.1 Contact forces

We consider spherical particles and the Hertz contact law [113] provides the repulsive force acting between them as a function of their overlap distance (Fig. 4.2). The repulsive force $\vec{F}_{ij}^{r}$ between spheres $i$ and $j$ depends on their relative position $\vec{r}_{ij} = \vec{r}_i - \vec{r}_j$, elastic moduli $E_i$ and $E_j$, Poisson ratios $\nu_i$ and $\nu_j$, and radii $R_i$ and $R_j$:

$$\vec{F}_{ij}^{r} = \begin{cases} \frac{4}{3} E R^{1/2} \xi_{ij}^{3/2} \, \hat{r}_{ij} & \xi_{ij} > 0, \\ 0 & \xi_{ij} \leq 0, \end{cases} \tag{4.1}$$

where $1/E = (1-\nu_i^2)/E_i + (1-\nu_j^2)/E_j$, $R = R_i R_j/(R_i + R_j)$ and $\xi_{ij} = R_i + R_j - r_{ij}$ and $\hat{r}_{ij} = \vec{r}_{ij}/r_{ij}$. (We symbolize unit vectors with the hat "^" notation.)

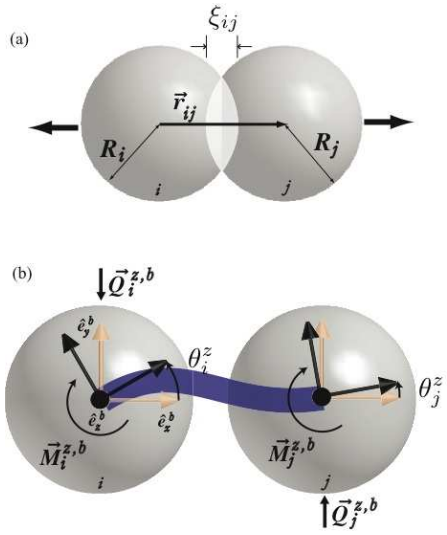


Figure 4.2: (a) Hertzian interaction of spherical elements. The repulsive contact force is given in Eq. (4.1). (b) Two particles connected by an elastic beam. The forces and torques arising at the centers of mass of the particles are calculated according to Equations (4.5, 4.6, 4.1).

A normal damping force and a tangential frictional force are included to the sphere-sphere interaction, acting only during each collision, that is, for $\xi_{ij} > 0$. The normal damping force depends on the normal component of the relative velocity $\vec{v}_{ij} = \vec{v}_i - \vec{v}_j$ and is given by:

$$\vec{F}_{ij}^d = -\gamma_n \left(\vec{v_{ij}} \cdot \hat{r}_{ij}\right) \hat{r}_{ij}. \tag{4.2}$$

The factor $\gamma_n$ is the normal damping coefficient and is assumed to be the same for all spheres.

The tangential friction force $\vec{F}_{ij}^s$ is proportional to the tangential component of the relative velocity of the surfaces $\vec{v}_{ij}^s$:

$$\vec{F}_{ij}^s = -\min\left(\gamma_s v_{ij}^s, \mu F_{ij}^d\right) \hat{v}_{ij}^s, \tag{4.3}$$

where

$$\vec{v}_{ij}^s = \vec{v}_{ij} - \left(\vec{v_{ij}} \cdot \hat{r}_{ij}\right) \hat{r}_{ij} - \frac{R_i\vec{\omega}_i + R_j\vec{\omega}_j}{R_i + R_j} \times \vec{r}_{ij}.$$

Here $\vec{\omega}_i$ and $\vec{\omega}_j$ are the angular velocities, $\gamma_s$ is the sliding friction coefficient and $\mu$ is the static friction coefficient, setting an upper limit to the tangential friction force to $\mu F_{ij}^d$.

In order to simulate impact, the elements also interact with walls. A wall with elastic modulus $E_p$ and Poisson ratio $\nu_p$, is specified by a point $\vec{p} = (x_1, x_2, x_3)$ that belongs to the plane, and the plane's normal vector $\hat{n} = (n_1, n_2, n_3)$. When a sphere is in contact with this plane, a repulsive force acts, normal to the plane, given by

$$\vec{F}^p = \begin{cases} \frac{4}{3} E^* R_i^{1/2} \xi^{3/2} \, \hat{n} & \xi > 0, \\ 0 & \xi \leq 0, \end{cases} \tag{4.4}$$

where $1/E^* = (1 - \nu_i^2)/E_i + (1 - \nu_p^2)/E_p$, and $\xi = R_i - r$, with $r$ being the distance from the center of the sphere to the plane surface (Fig. 4.3).

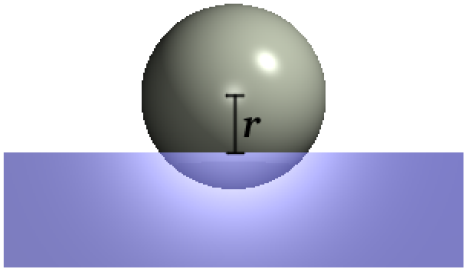


Figure 4.3: Interaction of a spherical element with a hard wall. The repulsive force acting on the particle is calculated using Eq. (4.4).

Again, frictional forces calculated as in Equations (4.2) and (4.3) are included in the simulations.

### 4.1.2 Cohesive forces

The spherical particles are connected by beams along the edges of a Delaunay triangulation of the initial positions of the particles. The 3D representation of beams used in this work is an extension of the two-dimensional case of Euler-Bernoulli beams described in Ref. [114]. In 3D the total deformation of a beam is calculated by the superposition of elongation, torsion, as well as bending and shearing in two different planes.

The restoring force acting on sphere $j$ connected by a beam to sphere $i$ due to the elongation of the beam is given by

$$\vec{F}_j^{elo} = -E^b A^b \varepsilon \hat{r}_{ij}, \tag{4.5}$$

where $E^b$ is the beam stiffness, $\varepsilon = (|\vec{r}_{ij}| - l_0)/l_0$, with the initial length of the beam $l_0$ and its cross section $A^b$.

The flexural forces and moments transmitted by a beam are calculated from the change in the orientations of each beam end, relative to the body-fixed coordinate system of the beam $(\hat{e}_x^b, \hat{e}_y^b, \hat{e}_z^b)$. Given the angles $\theta_i^z$ and $\theta_j^z$, the corresponding bending force $\vec{Q}_j^{z,b}$ and moment $\vec{M}_j^{z,b}$ for the elastic deformation of the beam are given by Ref. [114]:

$$\vec{Q}_j^{z,b} = 3E^b I \frac{(\theta_i^z + \theta_j^z)}{L^2} \hat{e}_y^b, \tag{4.6a}$$

$$\vec{M}_j^{z,b} = E^b I \frac{(\theta_i^z - \theta_j^z)}{L} \hat{e}_z^b + \left( \vec{Q}_i^{z,b} \times |\vec{r}_{ij}| \, \hat{e}_x^b \right), \tag{4.6b}$$

where $I$ is the beam moment of inertia. Corresponding equations are written for general rotations around $\hat{e}_y^b$, and the forces and moments are added up. Additional torsion moments are added to consider a relative rotation of the elements around $\hat{e}_x^b$:

$$\vec{M}_j^{x,b} = -G^b I^{tor} \frac{(\theta_j^x - \theta_i^x)}{L} \hat{e}_x^b, \tag{4.1}$$

with $G^b$ and $I^{tor}$ representing the shear modulus and moment of inertia of the beams along the beam axis, respectively. The bending forces and moments are transformed to the global coordinate system before they are added to the contact forces.

### 4.1.3 Breaking criterion

Overstressed beams can break in order to explicitly model damage, fracture, and failure of the solid. The imposed breaking rule takes into account breaking due to stretching and bending of a beam [88, 89, 91, 115, 116], which breaks if

$$\left( \frac{\varepsilon}{\varepsilon_{th}} \right)^2 + \frac{\max\left(|\theta_i|, |\theta_j|\right)}{\theta_{th}} \geq 1, \tag{4.2}$$

where $\varepsilon = \Delta l/l_0$ is the longitudinal strain, and $\theta_i$ and $\theta_j$ are the general rotation angles at the beam ends between elements $i$ and $j$, respectively. Here $\cos\theta_i = \hat{e}_x^{ib} \cdot \hat{e}_x^b$, where $(\hat{e}_x^{ib}, \hat{e}_y^{ib}, \hat{e}_z^{ib})$ define the $i-$particle's orientation in the beam body-fixed coordinate system. A similar calculation is performed to evaluate $\theta_j$. The criterion Eq. (4.2) has the same form as in the two-dimensional beam lattice presented in Chapter 3. Equation (4.2) is analogous to the von Mises yield criterion for metal plasticity [115, 117]. The first part of Eq. (4.2) refers to the breaking of the beam through stretching and the second through bending, with $\varepsilon_{th}$ and $\theta_{th}$ being the respective threshold values.

In discrete element simulations of fragmentation phenomena, spring or beam elements are allowed to break solely under tension [1]. In the original setup of our model used in Ref. [85], the breaking thresholds of beams $\varepsilon_{th}$ and $\theta_{th}$ are random variables characterized by Weibull distributions. Extensive computer simulations have revealed that this strength disorder of beams is irrelevant when structural disorder is present in the form of a random length, cross-section, ... of beams determined by the initial packing of particles. Therefore, in the present study the breaking thresholds for all the beams have fixed values at $\varepsilon_{th} = 0.03$ and $\Theta_{th} = 3$.

### 4.1.4 Time evolution

The time evolution of the system is obtained by numerically solving the equations of motion for the translation and rotation of all spheres using a $6^{th}$-order Gear predictor-corrector algorithm, and the dynamics of the rotations of the spheres is described using quaternions [83, 114]. The breaking rules are evaluated at each time step, removing those beams which fulfil the condition of Eq. (4.2). Beam breaking is irreversible, which means that broken beams are excluded from the force calculations for all future time. As a result of subsequent beam breakings, cracks develop in the sample which lead to fragmentation. The simulation is stopped when there is no beam breaking over 1000 consecutive time steps.

### 4.1.5 Simulation setup

We carried out MD simulations of the impact process varying the impact velocity $v_0$ in a broad range. We used four different system sizes with fixed

radii $R = 3.5, 5.63, 7.03, 8.12$ mm where the average radius of single particles is $\overline{r} = 0.5$ mm. The number of particles fluctuates in the samples about the average values $\langle N \rangle = 1763, 7337, 14285, 22013$. Fragments are identified in the final state as sets of particles connected by the surviving beams. Further details of the model construction together with the parameter settings and test simulations can be found in Ref. [85]. For impact fragmentation of spheres it has been shown in Ref. [85] that the experimentally observed dynamics of crack formation and breakup scenarios can be rather accurately reproduced by our DEM. In our study we focused on the transition from the damaged to the fragmented state in the impact induced breakup as the impact velocity is gradually increased.

## 4.2 Damage-fragmentation transition

In the limit of very low impact velocities no beam breaking is induced, i.e. the sample gets deformed and rebounds from the wall without any damaging. Simulations have shown that in this case the impact process can be described by the Hertz theory [118, 119]. The main characteristic quantities of the Hertz impact obey simple power law scaling with the impact velocity: the behavior of the maximum deformation $h \sim v_0^{4/5}$ and of the duration of contact $\tau \sim v_0^{-1/5}$ is reproduced by our DEM simulations with a good precision.

Increasing the impact velocity the sample gets damaged and gradually breaks into pieces. The degree of breakup can be quantitatively characterized by the mass of the largest fragment $M_{max}$ compared to the total mass of the body $M_{tot}$ [90, 91]. Simulations revealed that depending on the impact velocity the final outcomes of the breakup process of the spherical sample fall into two substantially different classes: at low impact velocities some cracks appear, however, the sample retains its integrity. Broken bonds form cracks which initiate from the contact surface with the hard wall, however, they get arrested without creating fragments or only some very small pieces are chopped out of the sample. Cracks are concentrated in a conical volume (Hertz cone [118, 119]), whose base is the contact circle with the hard wall. Consequently, in the final state of the process only small fragments comprising only a few spheres and a big residue can be observed [85]. This low velocity regime is the damage phase of the system, where the

mass of the largest fragment is practically equal to the total mass of the sample $M_{max}/M_{tot} \approx 1$. To achieve complete breakup the impact velocity has to exceed a threshold value $v_c$ above which even the largest fragment becomes significantly smaller than the original body $M_{max}/M_{tot} \ll 1$. This first happens when meridional cracks starting from the Hertz cone reach the surface of the sample opposite to the impact site [85]. Further increasing $v_0$, segmentation cracks are formed between meridional cracks further reducing the size of fragments [85].

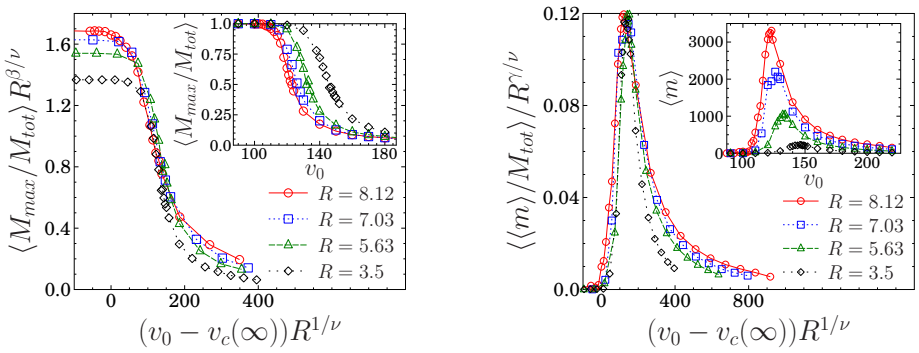


Figure 4.4: (*left*) Inset: mass of the largest fragment normalized by the total mass of the sample $\langle M_{max}/M_{tot}\rangle$ as a function of the impact velocity $v_0$ for different system sizes. Main panel: scaling collapse obtained by rescaling the two axis according to Eq. (4.5). (*right*) Inset: Average fragment mass as a function of the impact velocity for different system sizes. Main panel: Rescaling $\langle m\rangle$ and the impact velocity $v_0$ by an appropriate power of $R$, the curves corresponding to different system sizes collapse on a master curve.

The inset of Figure 4.4 (left) presents the sample average of the fraction of the largest fragment $\langle M_{max}/M_{tot}\rangle$ as a function of the impact velocity for the four different system sizes $R$ considered. It can be observed that the curves are monotonically decreasing and they have a curvature change whose position $v_c(R)$ can be identified with the transition point from the damaged to the fragmented regime [90, 91]. Note that with increasing system size $R$ the transition gets sharper and the transition point shifts to lower values typically observed for continues phase transitions. It has been shown in Ref. [90] that the strength of the largest fragment $\langle M_{max}/M_{tot}\rangle$ can be considered to be the order parameter of the transition.

The damage-fragmentation transition becomes more transparent by investigating the average mass of fragments $\langle m \rangle$ which is defined as the ratio of the second and first moments of fragment masses (see also Chapter 2)

$$\langle m \rangle = \langle M_2/M_1 \rangle \,. \tag{4.3}$$

$\langle m \rangle$ is obtained by averaging the ratio $M_2/M_1$ over a large number of simulations [90]. It can be observed in the inset of Fig. 4.4 (right) that $\langle m \rangle$ is strongly peaked which gets sharper with increasing $R$. We determined the finite size critical point $v_c(R)$ of the system as the position of the maximum of $\langle m \rangle$ which coincides with the point of curvature change of $\langle M_{max}/M_{tot} \rangle$ at a reasonable precision [112]. The critical velocities are $v_c(R_1) = 146$ m/s, $v_c(R_2) = 131$ m/s, $v_c(R_3) = 126$ m/s, $v_c(R_4) = 123.5$ m/s. Assuming the scaling form for the critical velocity

$$v_c(R) = v_c(\infty) + AR^{-1/\nu}, \tag{4.4}$$

in terms of the system size [94, 120] we determined numerically the critical velocity of the infinite system $v_c(\infty)$ and the correlation length exponent $\nu$ of the transition [112]. In Fig. 4.5 a power law is obtained with an excellent quality by setting $v_c(\infty) = 107$ m/s in Eq. (4.4).

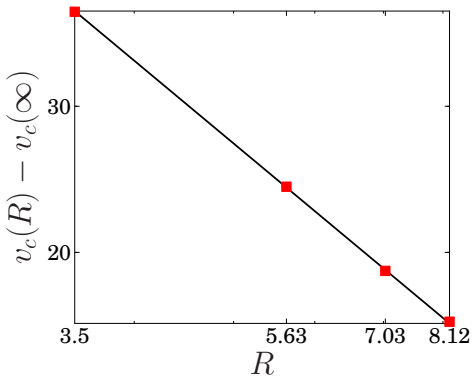


Figure 4.5: Difference of the critical value of the impact velocity of finite and infinite systems $v_c(R) - v_c(\infty)$ as a function of the system size $R$. The value of $v_c(\infty)$ was tuned to obtain the best quality power law according to Eq. (4.4).

The value of the exponent $\nu$ was obtained by fitting $\nu = 1 \pm 0.05$. The result implies that in the limit of very large system sizes the critical ve-

locity of the damage-fragmentation transition converges to $v_c(\infty)$. Starting from the finite size scaling of the critical velocity Eq. (4.4) we can analyze the size dependence of the normalized mass of the largest fragment. Since $\langle M_{max}/M_{tot}\rangle$ is the order parameter of the damage-fragmentation transition, it is reasonable to assume the scaling structure

$$\left\langle \frac{M_{max}}{M_{tot}} \right\rangle (v_0, R) = R^{-\beta/\nu} F^{(1)}((v_0 - v_c(\infty))R^{1/\nu}), \tag{4.5}$$

where $\beta$ is the order parameter critical exponent and $F^{(1)}$ denotes the scaling function. It can be observed in Fig. 4.4 (left) that rescaling the impact velocity $v_0$ and $\langle M_{max}/M_{tot}\rangle$ according to Eq. (4.5) the curves obtained at different system sizes can be collapsed with a reasonable accuracy. In Fig. 4.4 only the value of $\beta$ was tuned providing $\beta = 0.25 \pm 0.03$, while for $\nu$ and $v_c(\infty)$ the above values were inserted. It can also be seen in the figure that data collapse has the best quality in the vicinity of the transition point as it is expected [112].

The average fragment mass with the above definition characterizes the fluctuations of fragment masses [90, 94], hence, the finite size scaling analysis of $\langle m\rangle$ reveals the $\gamma$ exponent of the damage-fragmentation transition. Assuming that the system has a continuous phase transition, the scaling structure

$$\langle m\rangle = R^{\gamma/\nu} F^{(2)}((v_0 - v_c(\infty))R^{1/\nu}), \tag{4.6}$$

should hold [94, 120], where $F^{(2)}$ denotes the scaling function. Figure 4.4 (right) illustrates the good quality data collapse of the $\langle m\rangle$ curves which was obtained by inserting the above value of $\nu$ and $v_c(\infty)$ varying $\gamma$ as the only free parameter of the functional form Eq. (4.6). Best collapse was obtained with the exponent $\gamma = 0.1 \pm 0.02$. For consistency, we also checked for the largest system size the validity of the behavior $\langle m\rangle \sim |v_0 - v_c(R)|^{-\gamma}$, which proved to hold with the same $\gamma$ within the error bars [112].

## 4.3 Fragment mass distribution

The most important characteristic quantity of the fragmenting system is the mass distribution of fragments $p(m)$. It has been shown by experiments that $p(m)$ exhibits a power law behavior

$$p(m) \sim m^{-\tau} \tag{4.7}$$

for small masses $m \ll M_{tot}$ at and above the critical point $v_c$ [44, 45, 75, 95, 121, 122]. The most striking observation on fragmentation phenomena is the universality of the exponent $\tau$ of the mass distribution: fragmentation experiments on a large variety of heterogeneous materials have shown that the value of $\tau$ does not depend on materials' micro-structure, on the way the energy is imparted, and on the relevant length scale [54, 62, 95, 123, 124]. It is mainly determined by the dimensionality of the system [59, 74, 90] and by the mechanical response (brittle or ductile) of the sample [56]. DEM simulations of fragmentation processes have been able to reproduce the power law functional form [56, 59, 61, 74, 75, 85] with various types of cohesive interactions from Lennard-Jones solids [125, 126, 127, 128] through spring lattices [124, 128] to beam networks [74, 85, 93]. The concept of universality motivated the development of mechanism based stochastic models of fragmentation [77, 78], among which the crack branching-merging scenario proved to be the most successful [73, 76]. Recent DEM simulations of a generic model of brittle solids have reported a surprising result: the fragment mass exponent $\tau$ of a two-dimensional disc impacted against a hard wall was found to slowly increase with the imparted energy $E_0$. Based on the numerical analysis of the simulation data a logarithmic functional form was deduced $\tau \sim \ln E_0$ above the critical point [125, 129].

The universality of the mass distribution exponent $\tau$ is a crucial problem not solely from theoretical point of view but it has even practical importance in engineering design, e.g. when estimating the energy consumption or loading conditions in ore processing to achieve the desired size reduction. In order to settle the problem, we performed a large number of simulations for impact velocities above $v_c$ and carried out a scaling analysis of the mass distributions $p(m)$ for our largest system. In Ref. [85] it has been shown that for impact velocities slightly above $v_c$ the fragment mass distribution of impacting spheres is composed of two distinct parts: for small fragment masses a power law distribution is obtained with an exponential cutoff

$$p(m) \sim m^{-\tau} e^{-m/m_0} \tag{4.8}$$

while for the large ones $p(m)$ has a maximum which can be fitted with a Weibull or lognormal form. Here $m_0$ denotes the characteristic fragment mass. These outcomes are in agreement with the generic functional form proposed in Ref. [74] based on the stochastic nucleation of the first major

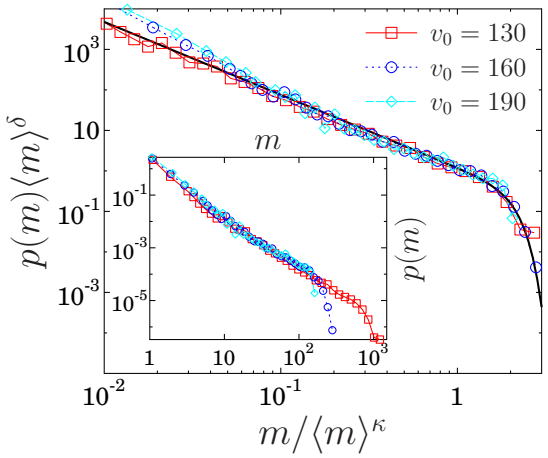


Figure 4.6: Inset: Mass distribution of fragments at different impact velocities for the largest system considered. Main panel: rescaling the two axis with appropriate powers of the average fragment mass a high quality data collapse is obtained.

cracks and the branching-merging scenario of the smaller ones. We selected impact velocities above $v_c$ where the disturbing effect of the surviving large pieces can be avoided. The inset of Fig. 4.6 presents mass distributions at three different impact velocities. It can be observed that they can qualitatively be described by the functional form Eq. (4.8). Note that as the impact velocity $v_0$ approaches $v_c$ from above the cutoff of the distributions moves towards larger values. To check whether the exponent $\tau$ of the distribution depends on $v_0$, we calculated the average fragment mass Eq. (4.3) and rescaled $p(m)$ with some powers of $\langle m\rangle$ along both axis. Figure 4.6 demonstrates that a high quality data collapse can be obtained with the scaling exponents $\kappa = 1.15 \pm 0.02$ and $\delta = 2.15 \pm 0.02$. The result implies that the fragment mass distributions $p(m, v_0)$ obtained at different impact velocities $v_0$ have the scaling structure

$$p(m, v_0) = \langle m\rangle^{-\delta}\, \Phi(m/\langle m\rangle^{\kappa}), \tag{4.9}$$

where the dependence on the impact velocity $v_0$ is comprised by $\langle m\rangle$ in the form $\langle m\rangle \sim |v_0 - v_c(R)|^{-\gamma}$. Since $\kappa \approx 1$, the scaling function $\Phi$ in Eq. (4.9) is consistent with Eq. (4.8) widely used in the literature. In Fig. 4.6 the bold black line was fitted using Eq. (4.8) from which the value of $\tau$ could

be determined accurately $\tau = 1.8 \pm 0.05$. It follows from the condition of normalization of the distributions, that the three exponents $\tau$, $\delta$, and $\kappa$ must fulfill the scaling relation

$$\delta = \tau\kappa. \tag{4.10}$$

Substituting the numerical values, it can be seen that the relation Eq. (4.10) holds with a good precision [112].

## 4.4 Time evolution of damage

The above analysis of the phase transition nature of fragmentation required the investigation of the final state of the breakup process. On the micro-level, cracks are generated by breaking beams such that fragments form when cracks either completely surround sets of particles connected by the surviving beams, or cracks span from surface to surface of the body. The total amount of broken beams and their spatial arrangement, i.e. crack structure, strongly depend on the impact velocity. The cracking mechanism leading to the formation of meridional and segmentation cracks of spherical bodies has been analyzed in details in Ref. [85]. Now we focus on the time evolution of damage which is quantified by the fraction of beams $D(t) = N_b(t)/N$ that has been broken up to time $t$. Here $N_b(t)$ denotes the number of broken beams at time $t$ and $N$ is the total number of beams in the sample. Of course, $D(t)$ is a monotonically increasing function ($0 \leq D(t) \leq 1$) whose derivative $dD/dt$ provides the rate of beam breaking characterizing the instantaneous breaking activity during the fragmentation process.

Breaking rate functions $dD/dt$ are presented in the inset of Fig. 4.7 for the largest system size $R_4 = 8.12$ mm at four different impact velocities $v_0$ in the damage phase $v_0 < v_c$. It can be observed in the figure that the increase of the impact velocity $v_0$ has a dramatic effect on the damage rate: $dD/dt$ has a maximum which becomes rapidly sharper and its position $t_m$ shifts towards lower time values with increasing $v_0$. Simulations showed that at the peak time $t_m$ the deformation of the contact zone of the sphere with the hard wall reaches its maximum value. It is important to emphasize that the breaking rate functions obtained at different impact velocities can be collapsed on a master curve by rescaling the two axis with some powers of $v_0$. In Figure 4.7 a high quality data collapse was obtained with the

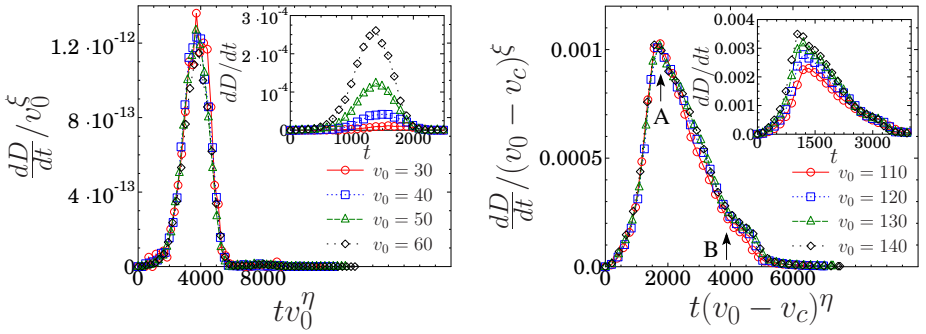


Figure 4.7: (*left*) Time evolution of the breaking rate $dD/dt$, for different values of the impact velocity below $v_c$. Rescaling the two axis with appropriate powers of $v_0$ excellent data collapse is obtained. The inset presents the original curves before rescaling.

exponents $\xi_d = 4.7 \pm 0.2$ and $\eta_d = 0.25 \pm 0.05$. The result implies that $dD/dt$ has the scaling structure

$$\frac{dD(t, v_0)}{dt} = v_0^{\xi} \Psi \left( t v_0^{\eta} \right), \tag{4.11}$$

where $\Psi$ denotes the scaling function.

Above the critical point $v_0 > v_c$ in the fragmented phase the damage rate reaches much higher values, i.e. it can be observed in the inset of Fig. 4.7 (right) that the functional form of $dD/dt$ is qualitatively the same as in the damage phase, however, with an order of magnitude larger values than in Fig. 4.7 (left). Simulations revealed that the peak time $t_m$ marks again the configuration where the compressive regime of the collision ends and unloading of the contact sets on. Along the decreasing branch of $dD/dt$ an inflexion point emerges at the time when all fragments rebound from the hard wall (see Fig. 4.7). It is demonstrated in Fig. 4.7 that the breaking rate functions obtained at different impact velocities can be again collapsed on a master curve by a rescaling transformation. Careful analysis of the simulated data showed that the scaling structure of $dD/dt$ is the same Eq. (4.11) as in the damage phase, however, when fragmentation is achieved the scaling variable is not simply the impact velocity $v_0$, but the distance from the critical point $v_0 - v_c$. The scaling exponents providing the best collapse in Fig. 4.7 were determined numerically as $\xi_f = 0.33 \pm 0.05$ and

$\eta_f = 0.11 \pm 0.02$.

A very important outcome of our scaling analysis is that the fragmentation process gets faster with increasing $v_0$, i.e. the characteristic time scale $t_c$ of the process has the behavior

$$t_c \sim v_0^{-\eta_d}, \quad \text{for} \quad v_0 < v_c, \tag{4.12}$$

$$t_c \sim (v_0 - v_c)^{-\eta_f}, \quad \text{for} \quad v_0 > v_c. \tag{4.13}$$

It is interesting to note that the functional form Eqs. (4.12, 4.13) is similar to the behavior of the contact time of the elastic collision of spherical bodies with a hard plate [118, 119]. In the damage phase $\eta_d$ falls close to the exponent of Hertz contacts $\eta_d \approx \eta_h = 0.2$, however, in the fragmented regime the strong energy dissipation gives rise to a slower decrease of $t_c$ characterized by a lower exponent $\eta_f < \eta_h$.

The total amount of damage $D_{tot}$ accumulated until the end of the fragmentation process can be obtained by integrating the damage rate $dD/dt(t, v_0)$ over time from 0 to infinity

$$D_{tot}(v_0) = \int_0^\infty \frac{dD}{dt}(t, v_0) dt. \tag{4.14}$$

Substituting the scaling form Eq. (4.11) it follows

$$D_{tot}(v_0) = v_0^\xi \int_0^\infty \Psi(v_0^\eta t) dt, \tag{4.15}$$

where the integral can be performed by exchanging the variable $t$ to $x = v_0^\eta t$. The calculations yield that the total amount of damage $D_{tot}$ has a power law dependence on $v_0$ in the damage phase

$$D_{tot} \sim v_0^\alpha, \tag{4.16}$$

while in the fragmentation phase a critical behavior is obtained

$$D_{tot} \sim (v_0 - v_c)^\alpha. \tag{4.17}$$

The critical exponent $\alpha$ of the total damage is determined by the two scaling exponents of the damage rate

$$\alpha = \xi - \eta, \tag{4.18}$$

which has different values $\alpha_d = \xi_d - \eta_d = 4.45$ and $\alpha_f = \xi_f - \eta_f = 0.22$ in the damage and fragmented states, respectively. The behavior of $D_{tot}$ is illustrated in Fig. 4.8, where we also fitted functions according to Eq. (4.16) and Eq. (4.17) in the damage and fragmented regimes, respectively. Best fits were obtained with the exponents 4.5 and 0.29 which agree very well with the above predictions. The high quality of the results presented in Fig. 4.8 demonstrates the consistency of our scaling analysis [112].

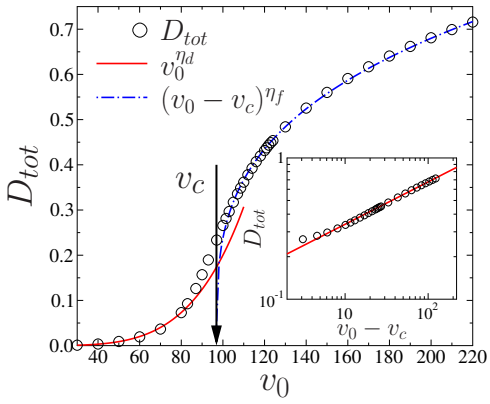


Figure 4.8: The total amount of damage $D_{tot}$ as a function of the impact velocity. The red (continuous) and blue (dotted-dashed) lines indicate the scaling laws Eq. (4.12) and Eq. (4.13) of the damage and fragmented states, respectively. The vertical arrow indicates the critical value of the impact velocity $v_c$. Inset: $D_{tot}$ as a function of $v_0 - v_c$, where $v_c = 98.5$ was used. A good quality power law behavior is obtained. The slope of the straight line is $\rho = 0.29$.

## 4.5 Conclusions

We investigated the fragmentation of spherical bodies due to impact with a hard wall focusing on the transition from the damaged to the fragmented state. We performed molecular dynamics simulations of a three-dimensional discrete element model at four different system sizes varying the impact velocity in a broad range. In order to determine the critical exponents of the transition, we carried out a finite size scaling analysis of the simulated data. The critical point of the transition from the damage to the fragmentation phase of finite size systems was identified with the impact velocity where

the average fragment mass takes a maximum value. Assuming the scaling structure characteristic for continuous phase transitions near the critical point, high quality data collapse was obtained for the mass of the largest fragment normalized by the total mass and for the average fragment mass. The scaling analysis proved the validity of the phase transition picture of impact fragmentation phenomena and yielded the critical exponents of the damage-fragmentation transition with a good accuracy [112].

Recent simulations of a generic model of fragmentation questioned the universality of the power law exponent of fragment mass distributions, predicting a logarithmic increase of the exponent with the imparted energy [125, 129]. In order to resolve this problem, we carefully analyzed the scaling behavior of fragment mass distributions obtained at different impact velocities. Although single distributions might suggest an apparent increase of the exponent, the high quality data collapse obtained by rescaling the distributions with the average fragment mass reveals universality [112].

In order to characterize the time evolution of the breakup process, we analyzed the scaling behavior of damage rate functions dD/dt obtained at different impact velocities. Based on the scaling structure of dD/dt, we showed that the total amount of damage increases as a power law of the impact velocity in the damage phase, however, in the fragmented regime power law is obtained as a function of the distance from the critical point. It is important to emphasize that this functional behavior is the consequence of the dimensionality of the system: in two dimensions DEM simulations provided a logarithmic dependence of the total damage with the impact velocity [91, 125, 129]. Our analysis revealed that in three dimensions the evolution of damage is characterized by power laws due to the Hertz type contact of the spherical body with the hard plate [112].

In the damaged and fragmented regimes the characteristic time scale of the breakup process was found to decrease as a power law of the impact velocity and of the distance from the critical point, respectively. When the sample retains its integrity (damage) the scaling exponent falls close to the exponent characterizing the velocity dependence of the duration of Hertz contacts. However, when fragmentation is achieved the exponent becomes significantly smaller, i.e. its value is nearly half of the Hertz exponent [112, 118, 119].

# Chapter 5

# Effect of plasticity on impact fragmentation

The concept of universality and the notion of an analogy to second order phase transitions in fragmentation phenomena have long been established and strongly supported by experimental findings. It is widely accepted that it is the effective dimensionality of the system that determines the value of the power law exponent of fragment mass distributions according to which universality classes of fragmentation can be distinguished. For heterogeneous bulk solids with a high degree of brittleness it has been shown that the main features of FSDs can be explained by the self-similar branching-merging scenario of propagating unstable cracks governed by tensile stresses. It is an interesting question how material properties such as plasticity affect the fragmentation process and how robust fragmentation universality classes are with regard to such properties. We present experimental results on the impact fragmentation of particles made of polypropylene (PP) and propose an extension of our previously used DEM approach to simulate the impact of plastic materials. The details of this work are published in Ref. [56].

## 5.1 Experiments

In the framework of an international collaboration I had the opportunity to participate in fragmentation experiments on plastic spheres. The experiments were carried out by Jan Blömer in the Fraunhofer Institute UMSICHT, Oberhausen, Germany. I participated in the evaluation of the ex-

perimental results. To perform impact fragmentation experiments a single particle comminution device was used which accelerates small spherical particles one-by-one by centrifugal force in a rotor up to the desired velocity. The device is built so that the particles hit the hard wall at a rectangular angle in an evacuated environment eliminating the disturbing effect of inclined impact and of turbulent air flow. In the experiments we used particles of diameter $d = 4$ mm made of isotactic polypropylene, which is a thermoplastic polymer with an intermediate level of crystallinity in its molecular structure. The most important parameters of PP are: Young's modulus 1300 $MPa$ (room temperature), glass transition temperature $-10\ ^oC$, melting point 160 $^oC$, and density 0.9 $g/cm^3$. Besides tacticity, the mechanical response and fracture characteristics of PP are also strongly affected both by the temperature and by the rate of loading: increasing strain rate gives rise to a more brittle response while raising the temperature enhances ductility [130]. Figure 5.1 shows our impact device from the side (left) and from the top (right).

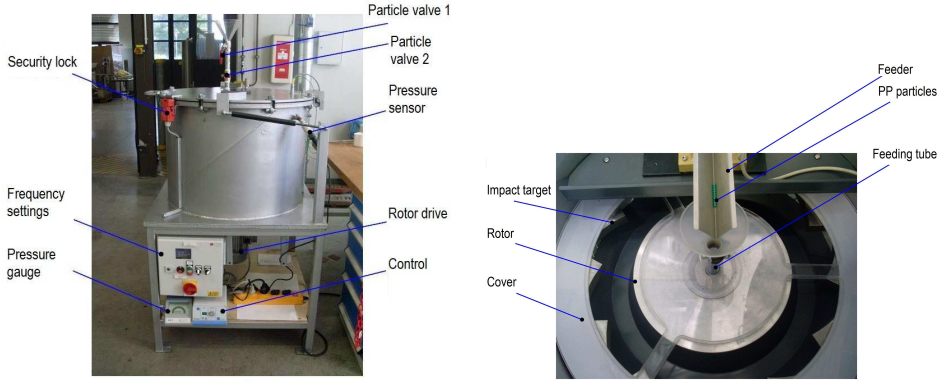


Figure 5.1: Side and top view of our single particle communition device, a specially designed rotor that catapults small PP particles against hard steel walls to achieve impact fragmentation.

We performed impact fragmentation experiments of spherical particles at different impact velocities $v_0$ in the range 30 m/s-180 m/s. Figure 5.2($a$) shows that at low enough velocities, the collision does not result in a breakup, instead the particles undergo a large plastic deformation at the impact site. Above the completely flattened contact zone of permanent deformation

meridional cracks form due to tensile stresses, however, the body does not fall apart, the plastic zone retains its integrity.

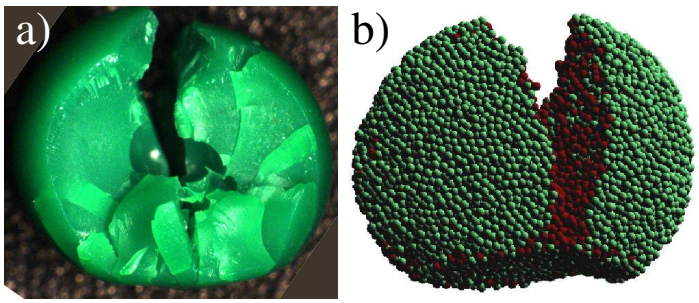


Figure 5.2: Final states of impact at low impact velocities in the experiment ($a$) and in the simulation ($b$). In the contact area with the hard wall large permanent deformations occur due to compression, while above it vertical cracks are formed due to tensile stresses. The simulations are in very good agreement with the measurements.

Fragmentation occurs when the impact velocity $v_0$ exceeds a material dependent critical value $v_c$, which is about 60m/s for our PP particles. At each impact velocity 400 particles were fragmented accumulating the fragments in the grinding chamber of the machine. In the data analysis, $99-99.5\%$ of the total mass of the samples was recovered. In order to evaluate the mass distribution of the fragments, we scanned the pieces with an open scanner obtaining digital images where fragments appear as white spots on the black background [59, 61]. This way the identification of fragments is reduced to cluster searching of white pixels. The very fine powder of extension smaller then the pixel size of the scanner was left out of the data analysis. The two-dimensional projected area $w$ of fragments is determined as the number of pixels of the clusters, from which the mass $m$ of fragments can be estimated as $m \sim w^{3/2}$ since the three-dimensional fragment shape is close to isotropic. We checked the shape isotropy by calculating the square root of the ratio of the larger $I_1$ and smaller $I_2$ eigenvalues of the tensor of inertia of the 2D projections. The inset of Fig. 5.3 shows that the value of $\sqrt{I_1/I_2}$ is close to 1.9 for almost all fragment masses indicating a high level of isotropy. The mass distribution $F(m)$ of fragments obtained at three different impact velocities is presented in Fig. 5.3.

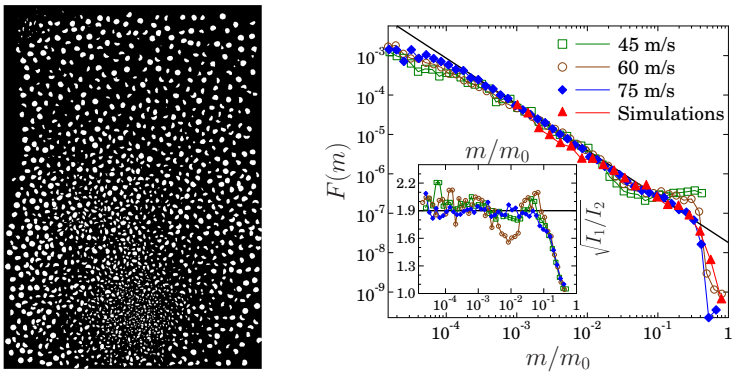


Figure 5.3: (*left*) Resulting fragments of our experiments of impact fragmentation of PP particles. The fragments are layed out on a scanner to analyze the properties of their 2D projection. (*right*) Mass distribution of fragments obtained from experiments at three different impact velocities. $m_0$ denotes the average mass of PP spheres. At the highest impact velocity $v_0 = 75$ m/s, $F(m)$ shows a power law behavior over 3 orders of magnitude followed by an exponential cutoff for the very large pieces. Simulation results obtained with the parameters $\Theta_{th} = 1$ and $t_h = 0$ (*bending&healing*) are in a very good agreement with the experimental findings. Inset: the shape parameter $\sqrt{I_1/I_2}$ of fragments as a function of mass for the experiments of the main figure.

It can be observed in the figure that at the highest impact velocity $v_0 = 75$ m/s, where the state of complete breakup is reached, a power law functional form emerges

$$F(m) \sim m^{-\tau_{pl}} \tag{5.1}$$

over more than 3 orders of magnitude in the regime of small fragments. At lower impact velocities the power law regime of the distribution is followed by a hump for the largest fragments which gradually disappears and the cutoff becomes exponential as $v_0$ increases. The most astonishing feature of the experimental results is that the value of the exponent $\tau_{pl} = 1.2 \pm 0.06$ of the power law regime is significantly lower than the values $\tau_{br} \approx 1.8 - 2.1$ typically found in the fragmentation of three-dimensional bulk objects consisting of disordered brittle materials [46, 62, 74, 75, 128]. The anomalously low value of $\tau_{pl}$ is the consequence of the breakup mechanism of plastic materials which has not been considered by the usual theoretical approaches [74, 128].

## 5.2 Bending and tension dominated breaking

In order to reveal the underlying physical mechanisms of the fragmentation of plastic materials, we used a DEM model to simulate the fragmentation of polymeric particles of spherical shape when they impact on a hard wall. The main ingredients of our model have already been discussed in the previous chapter. To be able to capture the deformation behaviour and fracture of plastic materials however, we need to add two novel features to the already existing model construction.

Cracks leading to fragmentation in brittle materials normally propagate as a result of tensile stresses and accordingly cracks tend to open up, i.e. crack surfaces are pulled away from each other. Therefore the restriction in our existing DEM model, that only elongated beams may break is valid in brittle systems usually dealt with in experiments. However in the case where material damage is a consequence of shear deformation, failure might occur even if there is a slight local compression present, as can be expected in an impact experiment. To take this into account we propose an extension of the breaking criterion in the form

$$\frac{\varepsilon|\varepsilon|}{\varepsilon_{th}^2} + \frac{\max\left(|\Theta_i|, |\Theta_j|\right)}{\Theta_{th}} \geq 1, \tag{5.2}$$

where the deformation $\varepsilon$ is not restricted to positive values. Since the first term of Eq. (5.2) becomes negative when the beam is compressed, failure is dominated by the bending/shear mode in such a way that increasing compression increases the shear resistance of the beam. It is important to emphasize that in the beam dynamics shear and bending are strongly coupled. It can be seen in Eq. 4.6 that shear deformation of a beam, i.e. relative displacement of the two beam ends in the direction perpendicular to the beam, imply torque which then results in bending angles. Simulations showed that the local shear of the particle contacts provides the main contribution to the bending angles $\theta_i$, $\theta_j$, so that bending dominated beam breaking in Eq. 5.2 characterizes crack formation due to shear. Varying the values of the breaking thresholds $\varepsilon_{th}$ and $\Theta_{th}$, the relative importance of stretching and bending can be controlled: increasing the value of a breaking parameter, the effect of the corresponding failure mode diminishes.

Another important feature in our approach in modeling plasticity is the

concept of healing. In order to represent the plastic behavior of the material, we assume that the beams have a linear elastic behavior up to fracture, but, whenever two particles are pressed against one another for a time longer than $t_h$, a new, undeformed beam is inserted between them. This way during the impact process, the particle contacts may undergo a sequence of breaking-healing events which leads to plastic energy dissipation and to the appearance of permanent deformation. Varying the healing time $t_h$ the mechanical response of the model material can be controlled: $t_h = 0$ corresponds to the case of perfect shear plasticity, while $t_h \to \infty$ implies no healing at all, i.e. brittle behavior.

In order to investigate the effect of local failure modes of beams on the fragmentation process, we carried out computer simulations by setting the stretching threshold to a fixed value $\varepsilon_{th} = 0.02$ and varying the bending threshold within a broad range $1.0 \leq \Theta_{th} \leq 200$. In this way $\Theta_{th} = 200$ and $\Theta_{th} = 1$ imply total tension and bending dominance, respectively, while intermediate $\Theta_{th}$ values interpolate between the two limits. Simulations were stopped when the system reached a relaxed state, i.e. no beam breaking occurred during 1000 consecutive time steps. Figure 5.2($b$) presents the final state of an impact simulation obtained with a sample of $N = 24000$ particles at low impact velocity. It can be observed that the model is able to reproduce both the deformation and the crack structure of PP, with parameter values where the beam breaking is dominated by bending $\Theta_{th} = 1.0$, furthermore, compressed contacts easily heal $t_h = 0$. The large permanent deformation of the sphere in Fig. 5.2($b$) arises due to breaking-healing sequences of particle contacts in the compressed impact zone. Above this zone tensile stresses arise resulting in opening cracks along the impact direction in agreement with the experiments.

We see in our simulations that a low bending threshold, i.e. low shear resistance will result in a lot of healing events simply due to the fact that in a bending-induced beam breaking the particles stay close to each other and have a high probability of meeting again, whereas in the high bending threshold limit, beams will break as a result of local tension corresponding to particles separating. Sequences of breaking-healing events in our impact simulations can be considered to represent the slip mechanisms in plastic materials resulting in permanent deformation [56].

## 5.3 Damage-fragmentation transition

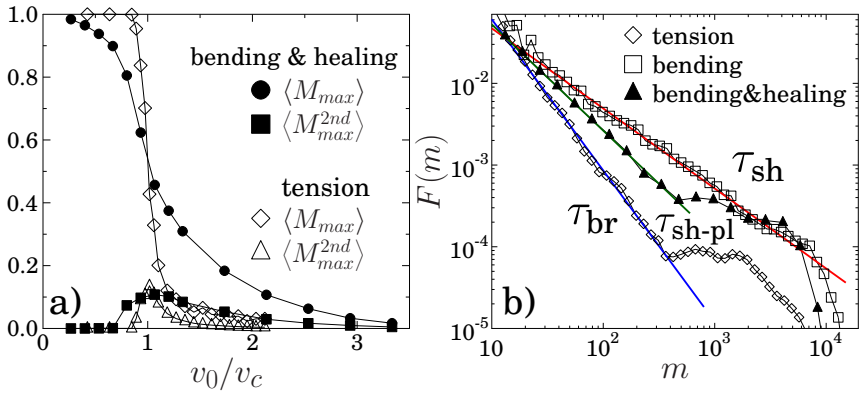


Figure 5.4: ($a$) The average mass of the largest $\langle M_{max}\rangle$ and second largest $\langle M^{2nd}_{max}\rangle$ fragments as a function of the impact velocity $v_0$ normalized by the critical velocity $v_c$ of fragmentation for two parameter sets. ($b$) Fragment mass distributions obtained for the limiting cases of tension, bending, and bending&healing dominated breakups giving the corresponding exponents $\tau_{br}$, $\tau_{sh}$, and $\tau_{sh-pl}$, respectively.

Figure 5.4($a$) presents the average mass of the largest $\langle M_{max}\rangle$ and second largest $\langle M^{2nd}_{max}\rangle$ fragments as a function of the impact velocity $v_0$ for the tension $\Theta_{th} = 200$ dominated brittle breakup $t_h = \infty$ (*tension*), and for the bending dominated fragmentation $\Theta_{th} = 1.0$ with perfect shear plasticity $t_h = 0$ (*bending&healing*). For low impact velocities the sample gets only damaged, hence, the largest fragment comprises nearly the entire mass $M_0$ of the body $\langle M_{max}\rangle \sim M_0$, while the second largest one is orders of magnitude smaller $\langle M^{2nd}_{max}\rangle \ll \langle M_{max}\rangle$. Fragmentation occurs when the largest and second largest pieces become comparable, i.e. at the critical velocity $v_c$ where the $\langle M^{2nd}_{max}\rangle$ curve has a maximum coinciding with the inflexion point of $\langle M_{max}\rangle$. Figure 5.4($a$) shows that for the breakup of brittle materials dominated by tensile stresses, the damage-fragmentation transition is sharp in agreement with experiments [44, 121], however, when shear breaking dominates a broad critical regime emerges. The reason is that at $v_c$ the largest fragment does not break up into large pieces as for the tension case, but

instead gradually erodes with a cleavage mechanism giving rise to a slowly decaying residue.

Representative examples for the mass distribution of fragments are presented in Fig. 5.4($b$) for three parameter sets. For the mass distribution of the tension dominated breakup of heterogeneous brittle materials obtained at the parameter values $\Theta_{th} = 200$, $t_h = \infty$ (*tension*) a power law behavior is evidenced with the usual exponent $\tau_{br} = 1.9 \pm 0.1$ [85]. Simulations showed that decreasing the healing time $t_h \to 0$ in the tension limit practically does not affect the fragmentation process because fragments are only generated by opening cracks which do not let healing play any role. It is important to emphasize that the breakup process substantially changes when shear dominates the crack formation $\Theta_{th} = 1$ (*bending*). Even in the case of perfectly brittle beam breaking $t_h = \infty$ the low shear resistance leads to a significantly lower exponent than in the tensile limit $\tau_{sh} = 1.0 \pm 0.05$ (see Fig. 5.4($b$)). Increasing the strength of plasticity $t_h \to 0$ when shear dominates the cracking $\Theta_{th} = 1$, the exponent of the fragment mass distribution slightly increases: due to the healing of cracks fragments can merge which decreases the relative frequency of large pieces leading to a faster decay of the distribution. The highest value of the exponent $\tau_{sh-pl} = 1.25 \pm 0.06$ is obtained in the plastic limit $t_h = 0$ together with $\Theta_{th} = 1.0$ (*bending& healing*). It is important to emphasize that varying solely the velocity of impact in Fig. 5.3, for the mass distribution of fragments an excellent agreement is obtained between the shear-plastic simulations and the experiments. The results show that the shear dominated cracking together with the healing mechanism of compressed crack surfaces are responsible for the unique fragmentation of plastic materials. During the impact process of the experiments a considerable fraction of the kinetic energy of the particle gets transformed into heat which enhances the effect of healing and plasticity in consistence with our theoretical results. Our extensive simulations indicate that the exponent $\tau_{sh-pl}$ is universal, i.e. it does not depend on the impact velocity or on materials' microstructure characterizing a novel universality class of fragmentation phenomena [56].

Due to low shear resistance, we find that the fragmentation of plastic shows similarities to the breakup of liquid droplets colliding with a wall. The spatial distribution of fragments and the crack structure in the final

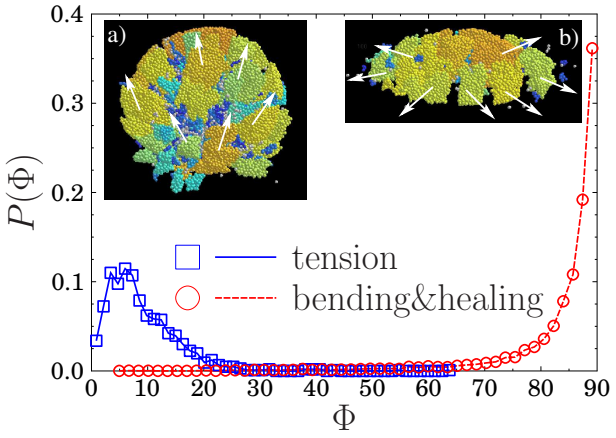


Figure 5.5: Probability distribution of the angle $\Phi$ between the velocity vector of fragments and the direction of impact for tension $\Theta_{th} = 200$ and shear $\Theta_{th} = 1.0$ dominated breakup. Insets: final states of fragmentation for tension ($a$) and shear ($b$) dominance. The arrows indicate the direction of the velocity of a few fragments.

state of brittle and plastic fragmentation are compared in the insets of Fig. 5.5. Although meridional and segmentation cracks are clearly observed in the brittle case in agreement with experiments, a lateral spreading of fragments is obtained for plastic with shear dominated breaking. For the quantitative characterization of the spatial spread of fragments, the distribution of the angle $\Phi$ of the velocity vector of fragments with the impact direction (vertical) is presented in Fig. 5.5. It can be observed that most of the fragments bounce back from the hard wall when tension dominates, however, in the shear-plastic case the fragments escape laterally producing a "splash" of the entire body similar to liquid droplets [54, 55].

## 5.4 Conclusions

Our experimental and theoretical study revealed that the breakup of plastic materials falls into a novel universality class of fragmentation phenomena characterized by the new mass distribution exponent [56]. Based on discrete element simulations we showed that the plastic behavior of the material together with the dominance of shear in crack formation are responsible for the substantial difference from brittle fragmentation. The low shear resistance of the material gives rise to a splashing similar to the breakup of

droplets of highly viscous liquids. Beyond the industrial importance of the fragmentation of polymeric materials, our results might also be applied to obtain a deeper understanding of the fragmentation of highly viscous magma during pyroclastic activity at volcanic eruption [42, 43]. For theoretical investigations our results demonstrate that the breakup of solids cannot be understood as a generic stochastic process since the precise mechanism of crack initiation and growth, i.e. the dominance of tensile or shear stresses govern the exponent of fragmentation. The challenge still remains to construct a theoretical approach which explains the emergence of universality based on crack dynamics.

# Chapter 6

# Summary

In the framework of my Ph.D. I studied the fracture and fragmentation of heterogeneous materials by means of molecular dynamics simulations of discrete element models. The first part of my thesis concentrated on the analysis of crackling noise emerging during the jerky propagation of a crack in three-point bending tests using a two-dimensional DEM. The fracture of heterogeneous materials have been long known to produce scale-invariant crackling noise due to the emergence of bursts/avalanches in crack propagation. My aim was to characterize various quantities related to such bursts and to investigate their dependence on disorder, i.e. the degree of brittleness of the sample. Also, I carried out a detailed study of the fracture process zone developing in front of the crack tip. The second part of my thesis was focused on the analysis of impact fragmentation of spherical bodies by using a three-dimensional discrete element model. Fragmentation of brittle materials are known to show universality in the form of power-law fragment mass distributions, with a universal exponent. It has been suggested that fragmentation phenomena can be considered analogous to continuous phase transitions. The goal of my studies was to achieve a clearer understanding of the fragmentation phase transition, to numerically obtain critical exponents and to investigate the scaling behaviour of damage below and above the transition point. I also addressed the important question of what effect plasticity has on the fragmentation process.

For the analysis of crackling noise in single crack propagation I used a two-dimensional discrete element model consisting of randomly shaped convex polygons that represent the granular structure of heterogeneous mate-

rials. The polygons are connected by elastic breakable beams with Weibull-distributed breaking thresholds. By varying the disorder in the threshold distributions (changing the Weibull exponent) I could control the degree of brittleness of the sample, low disorder corresponding to a high degree of brittleness. I carried out simulations of rectangular samples subject to three-point bending conditions, where a single crack would propagate in a stable manner. Before the onset of crack propagation the system accumulates a certain amount of damage in the form of uncorrelated micro-cracks, greatly depending on the degree of brittleness of the sample according to the simulations. A simple power-law formula was found for the dependence of the amount of damage on the Weibull exponent, for which I gave an analytic explenation in a mean-field type approximation. Simulations revealed that the crack propagates in a jerky manner as a result of a series of bursts/avalanches of beam breakings. A numerical technique was proposed to identify avalanches based on the temporal and spatial correlation of micro-fractures. I found a scale-invariant structure of the distributions of the size and duration of bursts and the waiting times in between them, i.e. a power-law functional form with an exponential cutoff. The value of the exponents have a reasonable agreement with recent experiments. Simulations revealed that ahead of the crack tip a process zone develops which is a sparse region of broken and intact elements. The fracture process zone proved to play an important role in the advancement of the crack: on the one hand the crack progresses by shrinking and expanding steps of the zone, on the other hand, micro- cracks can shield the stress field around the crack tip which helps to stabilize the system. The shrinking and expanding steps, i.e. the length of crack tip jumps and nucleation lengths also proved to follow power-law distributions. In the simulations I found a power-law decay of the damage profile with an exponential cutoff which is consistent with the assumption that the stress decay near the crack tip has a power-law form, as predicted by linear fracture mechanics.

For my studies on fragmentation, I used a three-dimensional DEM, in which the disordered structure of the solid is represented by a random packing of spherical elements of a bimodal size distribution. The spherical elements are connected by elastic beams which can be deformed due to stretching, bending and torsion. My simulations of the impact of brittle spheres

demonstrated that the exponent of the fragment mass distributions is independent of the impact velocity, strengthening the notion of universality. I carried out a finite size scaling analysis doing impact simulations with four different system sizes, and obtained a numerical approximation of the values of the critical exponents $\nu$, $\beta$ and $\gamma$ for three-dimensional brittle fragmentation. My results confirmed the validity of scaling relations regarding the mass $M_{max}$ of the largest fragment and the average fragment mass $\langle m \rangle$ previously suggested in two-dimensional brittle fragmentation. Analyzing the dependence of the characteristic time scale of the impact process on the impact velocity, I was able to reproduce Hertzian scaling behaviour for low velocities, i.e. in the damaged phase. For the fragmented phase however, simulations revealed a novel critical behaviour of the total accumulated damage and the damage rate as functions of the impact velocity. Above $v_c$ these quantities behave as powers of the distance from the critical velocity, as opposed to the logarithmic behaviour seen in two dimensions.

I investigated the effect of plasticity on impact fragmentation both experimentally and theoretically by proposing an extension of the previously used DEM to model plastic behaviour. Experiments of impact of small polypropylene particles were performed and the exponent of fragment mass distributions was found to be significantly smaller than that of brittle fragmentation. This striking result was confirmed by my simulations. I showed that the main characteristics of the impact of plastic spheres can be reproduced by molecular dynamics simulations by including some new model features, i.e. healing of beams and bending dominated breaking, facilitated by the new form of the breaking criterion. My results suggest that the fragmentation of brittle and plastic materials belong to distinct universality classes.

# Chapter 7

# Összefoglalás

Doktori tanulmányaim keretei közt rendezetlen szerkezetű anyagok törését és fragmentációját vizsgáltam diszkrét elem modellek molekuláris dinamikai szimulációja segítségével. Dolgozatom első részében a három-pontos hajlításos kísérletekben keletkező repedési zaj elemzésére vonatkozó eredményeimet mutatom be. Vizsgálataimat egy két-dimenziós diszkrét elem modell segítségével végeztem. Régóta ismert, hogy a rendezetlen szerkezetű anyagok törésében keletkező repedési zaj skála-invariáns szerkezetű, a repedés szakaszos, lavinákban történő előrehaladása miatt. Célom a különféle, lavinákkal kapcsolatos mennyiségek jellemzése, és rendezetlenségtől való függésének megállapítása volt. Emellett behatóan tanulmányoztam a repedés hegye előtt kialakuló process zóna viselkedését. Doktori dolgozatom második részében gömb-szerű testek becsapódási fragmentációjával foglalkoztam egy három-dimenziós diszkrét elem modell segítségével. A rideg anyagok fragmentációjának univerzális jellege régóta ismert tény, mely szerint a keletkező fragmens méret eloszlások hatványfüggvény viselkedést mutatnak, ahol az exponens rendszerint csak a rendszer dimenziójától függ. Számos eredmény utal arra, hogy a fragmentáció a folytonos fázisátalakulásokkal analóg jelenségnek tekinthető. Kutatásaim célja az volt, hogy tisztább képet kapjak a fragmentációs fázisátalakulásról és hogy numerikus módszerekkel meghatározzam az átalakulás kritikus exponenseit, valamint, hogy megvizsgáljam az anyagban keletkező sérülés skálaviselkedését a kritikus pont alatt és felett. Emellett behatóan foglalkoztam azzal a fontos kérdéssel, hogy hogyan befolyásolja a képlékenység a fragmentáció jelenségét.

A repedési zaj tulajdonságainak vizsgálatára egy két-dimenziós diszkrét

elem modellt használtam, melyben rendezetlen konvex poligonok reprezentálják a heterogén anyagok szemcsés szerkezetét. A poligonokat rugalmas, törhető rudak kötik össze, melyek törési küszöbei Weibull-eloszlásúak. A Weibull-exponens változtatásával kényelmesen változtatható a törési küszöbök rendezetlenségén keresztül az anyag ridegsége. Téglalap alakú testek három-pontos hajlítását szimuláltam, ahol egyetlen stabil repedés terjedését vizsgálhattam. A repedés megindulását megelőzően a rendszerben már fel tud halmozódni mikro-repedések formájában bizonyos mennyiségű sérülés. A szimulációk szerint az ily módon akkumulálódott sérülés mennyisége nagyban függ a rendszer ridegségétől. Egyszerű hatványfüggvény alakot találtam a felhalmozott sérülés mennyiségének a Weibull-exponenstől való függésére. A függés alakjára analitikus magyarázatot adtam egy átlagtér jellegű közelítésben. A szimulációim kimutatták, hogy a repedés szakaszosan terjed, rúd-törések kisebb-nagyobb lavináinak köszönhetően. A lavinák azonosítására kidolgoztam egy, a törések hely- és időbeli korrelációján alapuló numerikus módszert. A szimulációkban ily módon azonosított lavinák méretének, időtartamának és a lavinák között eltelt várakozási idők eloszlásának szerkezete skála-invariánsnak bizonyult, azaz hatványfüggvény alakúnak exponenciális levágással. A hatványfüggvény exponensek jó egyezést mutatnak a kisérletekkel. A szimulációk kimutatták, hogy a repedés hegye előtt kialakul egy törött és ép rudak váltakozásából álló szakasz, az ún. process zóna. A process zóna fontos szerepet játszik a repedés előrehaladásában: egyfelől a repedés a process zóna hirtelen, diszkrét lépésekben történő zsugorodása és növekedése révén halad előre, másrészt a process zónát alkotó mikro-repedések leárnyékolják a repedés hegye körül kialakuló feszültségteret, mely segít a rendszer stabilizálásában. A process zóna zsugorodási és növekedési lépéseinek nagyságai, vagyis a repedés ugrásainak hossza, és a nukleációs hosszak is hatványfüggvény alakú eloszlással rendelkeznek. A szimulációkban a sérülés-profil hatványfüggvény alakúnak adódott exponenciális levágással, ami konzisztens a lineáris törés-mechanika azon eredményével, hogy a feszültség lecsengése hatványfüggvény alakú a repedés hegyének közelében.

Fragmentáció vizsgálatára egy három-dimenziós diszkrét elem modellt használtam, melyben bimodális méreteloszlással rendelkező gömb alakú részecskék szoros illeszkedése alkotja a szilárdtest rendezetlen szerkezetét. A

részecskéket rugalmas rudak kötik össze, melyek nyújthatóak, hajlíthatóak és csavarhatóak. Rideg gömbök becsapódását szimulálva azt tapasztaltam, hogy a fragmens méret eloszlás exponense független a becsapódási sebességtől, ami erősíti az univerzalitás fogalmának érvényességét. Négy különböző rendszerművel végzett szimulációk alapján véges méret skálázás segítségével sikerült jó pontossággal meghatároznom a $\nu$, $\beta$ és $\gamma$ kritikus exponensek értékeit három-dimenziós rideg fragmentáció esetére. Eredményeim megerősítették a legnagyobb $M_{max}$ és az átlagos $\langle m \rangle$ fragmenstömegre vonatkozó skálarelációk érvényességét, melyeket eddig behatóan csak két dimenzióban vizsgáltak. A becsapódási folyamat karakterisztikus időskálájának a becsapódási sebességtől való függését vizsgálva azt tapasztaltam, hogy a szimulációim visszaadják a Hertz-féle skálaviselkedést alacsony sebességekre, azaz a sérült fázisban. A fragmentált fázisban viszont a teljes felhalmozódott sérülés és ennek idő szerinti deriváltja is újszerű, kritikus viselkedést mutat a becsapódási sebesség függvényeként. A kritikus sebesség fölött ezek a mennyiségek a kritikus sebességtől való távolság hatványaként változnak, a két dimenzióban tapasztalt logaritmikus viselkedéstől eltérően.

Tanulmányoztam a képlékenység hatását a becsapódási fragmentációra kísérletileg és elméletileg, a már meglévő diszkrét elem modell alkalmas kiegészítésével. Becsapódási kísérleteket végeztünk kis polipropilén részecskékkel és azt tapasztaltuk, hogy a fragmens méreteloszlás exponense lényegesen kisebbnek adódott a rideg anyagokkal végzett kísérletekben mértekhez képest. Ezt a meglepő eredményt sikerült a szimulációimmal is alátámasztani. Megmutattam, hogy a képlékeny anyagok becsapódási fragmentációjának legfontosabb jellemzői reprodukálhatóak a szimulációkban, néhány fontos modell kiegészítéssel: törött rudak újraéledésével, és a módosított törési kritérium által elősegített hajlítás által dominált rúdtörésekkel. Eredményeim szerint a rideg és képlékeny anyagok fragmentációja külön univerzalitási osztályba tartozik.

# Chapter 8

# Publications

**Refereed journals**

1. *Scaling Laws of Impact Fragmentation of Spherical Bodies*
   G. Timár, F. Kun, H. A. Carmona and H. J. Herrmann
   (submitted to Physical Review E)

2. *Crackling Noise in Three-Point Bending of Heterogeneous Materials*
   Gábor Timár and Ferenc Kun
   Physical Review E **83**, 046115 (2011)

3. *Crackling Noise in a Discrete Element Model of Single Crack Propagation*
   Gábor Timár and Ferenc Kun
   Computer Methods in Materials Science **11**, 309-314 (2011)

4. *New Universality Class for the Fragmentation of Plastic Materials*
   G. Timár, J. Blömer, F. Kun, and H. J. Herrmann
   Physical Review Letters **104**, 095502 (2010)

5. *The Effect of Disorder on Crackling Noise in Fracture Phenomena*
   Zoltán Halász, Gábor Timár and Ferenc Kun
   Progress of Theoretical Physics Supplement **184**, 385 (2010)

**Other publications**

1. *Fragmentation of Plastic Materials*
   Gábor Timár, Ferenc Kun, Jan Blömer and Hans J. Herrmann
   Acta Physica Debrecina XLV, 228 (2011)

2. *Crackling Noise in the Three-Point Bending of Heterogeneous Materials*
   Gábor Timár and Ferenc Kun
   Acta Physica Debrecina XLIV, 168 (2010)

**Poster**

1. *Crackling noise during single crack propagation*
   Gábor Timár and Ferenc Kun
   MECO 35 "Middle European Cooperation in Statistical Physics",
   Pont-á-Mousson, France, March 15-19. 2010.

**Talks**

1. *Crackling Noise in a Discrete Element Model of Single Crack Propagation*
   Gábor Timár and Ferenc Kun
   XVIII Komplastech Conference (Computer Methods in Materials Technology),
   Zakopane, Poland, January 16-19. 2011.

2. *Zajos repedésterjedés*,
   Gábor Timár and Ferenc Kun
   Statisztikus Fizikai Nap,
   Budapest, Hungary, March 22. 2010.

3. *Crackling noise in dynamic fracture*,
   Gábor Timár and Ferenc Kun
   1st Debrecen Workshop on the Statistical Physics of Fracture and Related Problems,
   Debrecen, Hungary, February 8-9. 2010.

4. *Képlékeny anyagok fragmentációja*
   Gábor Timár and Ferenc Kun
   Statisztikus Fizikai Nap,
   Budapest, Hungary, April 16. 2009.

5. *Discrete element model for impact fragmentation*
   G. Timár, H. J. Herrmann and F. Kun
   AIF project meeting,
   Fraunhofer UMSICHT, Oberhausen, Germany, May 5. 2008.

6. *Simulation of impact fragmentation in 3D*
   G. Timár, H. J. Herrmann and F. Kun
   Physical Aspects of Fracture Scaling and Size Effects,
   Monte Veritá, Ascona, Switzerland, March 9-14. 2008.

7. *Effect of plasticity on impact fragmentation*,
   G. Timár, H. J. Herrmann and F. Kun
   Weekly seminar, Computational Physics for Engineering Materials, IfB
   ETH Zürich, Switzerland, October 3. 2007.

**Acknowledgements**

I would like to express my gratitude to all the people who have helped me during my research as a Ph.D. student.

This thesis would not have been possible without the help, support and patience of my supervisor, Ferenc Kun. I am indebted to him for his guidance and encouragement throughout the years of my Ph.D. studies.

I am most grateful to Hans Herrmann, Humberto Carmona, Jan Blömer and Zoltán Halász for their collaboration which has been invaluable. Finally I would like to thank all the members of the Department of Theoretical Physics of the University of Debrecen for providing a perfect atmosphere for my Ph.D. research.

The work/publication is supported by the TÁMOP-4.2.2/B-10/1-2010-0024 project. The project is co-financed by the European Union and the European Social Fund.

# Bibliography


[1] H. J. Herrmann and S. Roux, *Statistical models for the fracture of disordered media, Random materials and processes* (North Holland, Amsterdam, 1990).

[2] A. A. Griffith, Philos. T. Roy. Soc. A **221**, 163 (1920).

[3] A. A. Griffith, Proceedings of the First International Conference of Applied Mechanics, Delft , 55 (1924).

[4] G. R. Irwin, J. Appl. Mech-T. ASME **24**, 361 (1957).

[5] G. R. Irwin, J. Appl. Mech-T. ASME **29**, 651 (1962).

[6] Z. P. Bazant, Proc. Natl. Acad. Sci. U.S.A. **101**, 13400 (2004).

[7] B. Lawn, *Fracture of Brittle Solids (Cambridge Solid State Science Series)* (Cambridge University Press, 1993).

[8] A. Johansen and D. Sornette, Eur. Phys. J. B **18**, 163 (2000).

[9] M. Alava, P. K. Nukala, and S. Zapperi, Adv. in Phys. **55**, 349 (2006).

[10] E. T. Lu, Phys. Rev. Lett. **74**, 2511 (1995).

[11] J. P. Sethna, K. A. Dahmen, and C. R. Myers, Nature **410**, 242 (2001).

[12] G. Durin and S. Zapperi, Phys. Rev. Lett. **84**, 4705 (2000).

[13] D. Spasojević, S. Bukvić, S. Milošević, and H. E. Stanley, Phys. Rev. E **54**, 2531 (1996).

[14] R. A. White and K. A. Dahmen, Phys. Rev. Lett. **91**, 085702 (2003).

[15] C. Maes, A. Van Moffaert, H. Frederix, and H. Strauven, Phys. Rev. B **57**, 4987 (1998).

[16] A. Petri, G. Paparo, A. Vespignani, A. Alippi, and M. Costantini, Phys. Rev. Lett. **73**, 3423 (1994).

[17] L. I. Salminen, A. I. Tolvanen, and M. J. Alava, Phys. Rev. Lett. **89**, 185503 (2002).

[18] M. Kloster, A. Hansen, and P. C. Hemmer, Phys. Rev. E **56**, 2615 (1997).

[19] M. C. Miguel, A. Vespignani, S. Zapperi, J. Weiss, and J. Grasso, Nature (London) **410**, 667 (2001).

[20] S. Field, J. Witt, F. Nori, and X. Ling, Phys. Rev. Lett. **74**, 1206 (1995).

[21] S. Deschanel, L. Vanel, N. Godin, G. Vigier, and S. Ciliberto, J. Stat. Mech. , P01018 (2009).

[22] F. Kun, G. B. Lenkey, N. Takács, and D. L. Beke, Phys. Rev. Lett. **93**, 227204 (2004).

[23] G. Niccolini *et al.*, Phys. Rev. E **80**, 026101 (2009).

[24] A. Corral, Phys. Rev. Lett. **92**, 108501 (2004).

[25] J. Davidsen, S. Stanchits, and G. Dresen, Phys. Rev. Lett. **98**, 125502 (2007).

[26] L. de Arcangelis, S. Redner, and H. J. Herrmann, J. Phys. (Paris), Lett. **46**, 585 (1985).

[27] S. Zapperi, P. K. V. V. Nukala, and S. Šimunović, Phys. Rev. E **71**, 026106 (2005).

[28] M. J. Alava, P. K. V. V. Nukala, and S. Zapperi, Phys. Rev. Lett. **100**, 055502 (2008).

[29] P. C. Hemmer and A. Hansen, ASME J. Appl. Mech. **59**, 909 (1992).

[30] A. Hansen and P. C. Hemmer, Phys. Lett. A **184**, 394 (1994).

[31] S. Pradhan, A. Hansen, and P. C. Hemmer, Phys. Rev. Lett. **95**, 125501 (2005).

[32] S. Pradhan, A. Hansen, and P. C. Hemmer, Phys. Rev. E **74**, 016122 (2006).

[33] F. Kun, S. Zapperi, and H. J. Herrmann, Eur. Phys. J. B **17**, 269 (2000).

[34] R. C. Hidalgo, F. Kun, and H. J. Herrmann, Phys. Rev. E **64**, 066122 (2001).

[35] F. Kun and S. Nagy, Phys. Rev. E **77**, 016608 (2008).

[36] F. Raischel, F. Kun, and H. J. Herrmann, Phys. Rev. E **77**, 046102 (2008).

[37] R. Kienzler and W. Schmitt, Powder Technology **61**, 29 (1990).

[38] S. K. Moothedath and S. C. Ahluwalia, Powder Technology **71**, 229 (1992).

[39] H. Rumpf, Powder Technology **7**, 145 (1973).

[40] M. Yoda, K. Tamura, A. Hashimoto, and Y. Sato, Powder Technology **52**, 171 (1987).

[41] A. Carpinteri, G. Lacidogna, and N. Pugno, International Journal of Fracture **129**, 131 (2004).

[42] I. Sugioka and M. Bursik, Nature **373**, 689 (1995).

[43] M. Alidibirov and D. B. Dingwell, Nature **380**, 146 (1996).

[44] T. Kadono, Phys. Rev. Lett. **78**, 1444 (1997).

[45] T. Kadono and M. Arakawa, Phys. Rev. E **65**, 035107 (2002).

[46] L. Oddershede, P. Dimon, and J. Bohr, Phys. Rev. Lett. **71**, 3107 (1993).

[47] S. Wu, Powder Technology **144**, 41 (2004).

[48] A. O. Gates, Trans. Am. Inst. Min. Metall. Pet. Eng. **52**, 875 (1915).

[49] A. M. Gaudin, Trans. Am. Inst. Min. Metall. Pet. Eng. **73**, 253 (1926).

[50] R. Schuhmann, Trans. Am. Inst. Min. Metall. Pet. Eng., Mining Technology **4**, 1 (1940).

[51] D. L. Turcotte, J. of Geophys. Res. **91**, 1921 (1986).

[52] D. L. Turcotte, *Fractals and Chaos in Geology and Geophysics* (Cambridge University Press, 1992).

[53] B. R. Lawn and T. R. Wilshaw, *Fracture of Brittle Solids* (Cambridge University Press, 1975).

[54] E. Villermaux, Annu. Rev. Fluid Mech. **39**, 419 (2007).

[55] C. F. Moukarzel, S. F. Fernández-Sabido, and J. C. Ruiz-Suárez, Phys. Rev. E **75**, 061127 (2007).

[56] G. Timár, J. Blömer, F. Kun, and H. J. Herrmann, Phys. Rev. Lett. **104**, 095502 (2010).

[57] M. Matsushita and T. Ishii, Department of Physics, Chuo University (1992).

[58] M. Matsushita and K. Sumida, Chuo University **31**, 69 (1981).

[59] F. Wittel, F. Kun, H. J. Herrmann, and B. H. Kröplin, Phys. Rev. Lett. **93**, 035504 (2004).

[60] F. K. Wittel, F. Kun, H. J. Herrmann, and B. H. Kröplin, Phys. Rev. E **71**, 016108 (2005).

[61] F. Kun, F. K. Wittel, H. J. Herrmann, B. H. Kröplin, and K. J. Måløy, Phys. Rev. Lett. **96**, 025504 (2006).

[62] A. Meibom and I. Balslev, Phys. Rev. Lett. **76**, 2492 (1996).

[63] N. Arbiter, C. C. Harris, and G. A. Stamboltzis, T. Soc. Min. Eng. **244**, 118 (1969).

[64] A. D. Salman *et al.*, Powder Technology **128**, 36 (2002).

[65] A. D. Salman and D. A. Gorham, Powder Technology **107**, 179 (1999).

[66] N. F. Mott, Ministry of Supply, Report No. AC 3642 (1943).

[67] N. F. Mott, Ministry of Supply, Report No. AC 4035 (1943).

[68] H. Katsuragi, D. Sugino, and H. Honjo, Proc. R. Soc. London, Ser. A **189**, 300 (1943).

[69] N. F. Mott and E. H. Linfoot, Ministry of Supply, Report No. AC 3348 (1943).

[70] D. E. Grady and M. E. Kipp, J. Appl. Phys. **58**, 1210 (1985).

[71] J. J. Gilvarry, J. Appl. Phys. **32**, 391 (1961).

[72] J. J. Gilvarry and B. H. Bergstrom, J. Appl. Phys. **32**, 400 (1961).

[73] J. Åström and J. Timonen, Phys. Rev. Lett. **78**, 3677 (1997).

[74] J. A. Åström, F. Ouchterlony, R. P. Linna, and J. Timonen, Phys. Rev. Lett. **92**, 245506 (2004).

[75] J. A. Åström, R. P. Linna, J. Timonen, P. F. Møller, and L. Oddershede, Phys. Rev. E **70**, 026104 (2004).

[76] P. Kekäläinen, J. A. Åström, and J. Timonen, Phys. Rev. E **76**, 026112 (2007).

[77] A. Levandovsky and A. C. Balazs, Phys. Rev. E **75**, 056105 (2007).

[78] S. J. Steacy and C. G. Sammis, Nature **353**, 250 (1991).

[79] C. G. Sammis, G. King, and R. Biegel, Pure Appl. Geophys. **125**, 777 (1987).

[80] H. J. Herrmann and S. Roux, *S. Redner, in: Statistical Models for the Fracture of Disordered Media, Random materials and processes* (Elsevier Science B.V., 1990).

[81] T. W. Peterson and M. V. Scotto, Powder Technology **45**, 87 (1985).

[82] R. C. Hidalgo and I. Pagonabarraga, Europhys. Lett. **77**, 64001 (2007).

[83] D. C. Rapaport, *The Art of Molecular Dynamics Simulations* (Cambridge University Press, Cambridge, 2004).

[84] P. L. Garrido and J. Marro, *3rd Granada Lectures in Computational Physics* (Springer, Heidelberg, 1995).

[85] H. A. Carmona, F. K. Wittel, F. Kun, and H. J. Herrmann, Phys. Rev. E **77**, 051302 (2008).

[86] K. B. Lauritsen, H. Puhl, and H. J. Tillemans, Int. J. of Mod. Phys. C **5**, 909 (1994).

[87] H. J. Tillemans and H. J. Herrmann, Physica A **217**, 261 (1995).

[88] F. Kun and H. J. Herrmann, Comput. Methods Appl. Mech. Eng. **138**, 3 (1996).

[89] F. Kun and H. J. Herrmann, Int. J. Mod. Phys. C **7**, 837 (1996).

[90] F. Kun and H. J. Herrmann, Phys. Rev. E **59**, 2623 (1999).

[91] B. Behera, F. Kun, S. McNamara, and H. J. Herrmann, J. Phys. Cond. Mat. **17**, 2439 (2005).

[92] M. P. Allen and D. J. Tildesley, *Computer Simulation of Liquids* (Oxford University Press, Oxford, 1984).

[93] G. A. D'Addetta, F. Kun, and E. Ramm, Granular Matter **4**, 77 (2002).

[94] D. Stauffer and A. Aharony, *Introduction to Percolation Theory* (Taylor & Francis, 1992).

[95] H. Katsuragi, D. Sugino, and H. Honjo, Phys. Rev. E **68**, 046105 (2003).

[96] H. Katsuragi, D. Sugino, and H. Honjo, Phys. Rev. E **70**, 065103(R) (2004).

[97] G. Timár and F. Kun, Phys. Rev. E **83**, 046115 (2011).

[98] G. Timár and F. Kun, Computer Methods in Materials Science **11**, 309 (2011).

[99] Z. Halász, G. Timár, and F. Kun, Progress of Theoretical Physics Supplement **184**, 385 (2010).

[100] G. Niccolini, G. Durin, A. Carpinteri, G. Lacidogna, and A. Manuello, J. Stat. Mech. **01023** (2009).

[101] Z. P. Bazant and J. Planas, *Fracture and size effect in concrete and other quasibrittle materials* (CRC Press, Boca Raton, FL, 1997).

[102] N. M. Pugno and R. S. Ruoff, Phil. Mag. **84**, 2829 (2004).

[103] N. M. Pugno, Int. J. Fract. **140**, 159 (2006).

[104] N. M. Pugno, Int. J. Fract. **141**, 311 (2006).

[105] N. M. Pugno, A. Carpinteri, M. Ippolito, A. Mattoni, and L. Colombo, Eng. Fract. Mech. **75**, 1794 (2008).

[106] M. J. Alava, P. K. V. V. Nukala, and S. Zapperi, J. Phys. D: Appl. Phys. **42**, 214012 (2009).

[107] N. M. Pugno, J. Phys.: Condens. Matter **18**, S1971 (2006).

[108] N. M. Pugno, Small **18**, S1971 (2008).

[109] F. Bosia, M. J. Buehler, and N. M. Pugno, Phys. Rev. E **82**, 056103 (2010).

[110] N. M. Pugno, F. Bosia, and A. Carpinteri, Meas. Sci. Technol. **20**, 084028 (2009).

[111] N. M. Pugno and F. Bosia, Nanotechnology Magazine, IEEE **3**, 14 (2009).

[112] G. Timár, F. Kun, H. A. Carmona, and H. J. Herrmann, submitted to Phys. Rev. E (2012).

[113] L. D. Landau and E. M. Lifshitz, *Theory of Elasticity, vol. 7 of Course of Theoretical Physics* (Butterworth-Heinemann, London, 1986).

[114] T. Poschel and T. Schwager, *Computational Granular Dynamics: Models and Algorithms* (Springer-Verlag, Berlin Heidelberg New York, 2005).

[115] H. J. Herrmann, A. Hansen, and S. Roux, Phys. Rev. B **39**, 637 (1989).

[116] G. A. D'Addetta, F. Kun, E. Ramm, and H. J. Herrmann, *Continuous and Discontinuous Modelling of Cohesive-Frictional Materials* (Springer-Verlag, Berlin, 2001).

[117] G. Lilliu and J. G. M. van Mier, Eng. Fract. Mech. **70**, 927 (2003).

[118] K. L. Johnson, *Contact Mechanics* (Cambridge University Press, New York, 1985).

[119] W. J. Stronge, *Impact Mechanics* (Cambridge University Press, New York, 2000).

[120] H. Nishimori and G. Ortiz, *Elements of Phase Transitions and Critical Phenomena* (Oxford University Press, Oxford, 2011).

[121] H. Katsuragi, S. Ihara, and H. Honjo, Phys. Rev. Lett. **95**, 095503 (2005).

[122] F. P. M. dos Santos, V. C. Barbosa, R. Donangelo, and S. R. Souza, Phys. Rev. E **81**, 046108 (2010).

[123] K. T. Chau, X. X. Wei, R. H. C. Wong, and T. X. Yu, Mechanics of Materials **32**, 543 (2000).

[124] H. Inaoka, E. Toyosawa, and H. Takayasu, Phys. Rev. Lett. **78**, 3455 (1997).

[125] N. Sator and F. Sausset, Europhys. Lett. **81**, 44002 (2008).

[126] A. Diehl, H. A. Carmona, L. E. Araripe, J. S. Andrade, and G. A. Farias, Phys. Rev. E **62**, 4742 (2000).

[127] C. D. Lorenz and M. J. Stevens, Phys. Rev. E **68**, 021802 (2003).

[128] J. A. Åström, B. L. Holian, and J. Timonen, Phys. Rev. Lett. **84**, 3061 (2000).

[129] N. Sator and H. Hietala, Int. J. Fract. **163**, 101 (2010).

[130] H. Saechtling, J. Haim, and D. Hyatt, *Saechtling International Plastics Handbook: For the Technologist, Engineer and User* (Hanser Gardner Publications, 1995).